Design and Analysis of an Innovative run-flat system for pneumatic tires

Abhishek Saraswat

Thesis submitted to the faculty of the Virginia Polytechnic Institute and State University
in partial fulfillment of the requirements for the degree of

Master of Science
In
Mechanical Engineering

Saied Taheri, Chair
Robert West
Romesh Batra

September 27, 2024
Blacksburg, Virginia

Keywords: Run-Flat Tires, ABAQUS, Rubber Fatigue

Design and Analysis of an Innovative run-flat system for pneumatic tires

Abhishek Saraswat

ABSTRACT

Pneumatic tires have been an essential part of the automobile since the early 20th century. Providing load carrying, braking, accelerating and turning capability as well as a certain degree isolation from the road, they fail to function without the presence of air pressure inside them. Run-flat tire systems allow the vehicle to continue running with reduced driving speeds for a certain specified range in case of loss of air pressure due to puncture or damage. In this work, the design of self-supporting and insert supported run-flat systems was approached using CAE.

Two tire FE models of sizes 175/70 R14 and 175/60 R18 were used in this study. All structural and thermal simulations were done using ABAQUS and ENDURICA software was used for fatigue life simulation. Distance travelled before failure was used as the primary parameter for design evaluation along with secondary parameters of contact patch area and contact pressure, tire temperature profiles and rolling resistance. Ride comfort and handling characteristics are important performance parameters for a tire. Thus, a limited study to quantify the effect of run-flat system on the ride and handling properties was also conducted. The target design values for maximum load were fixed according to ETRTO standards while the maximum operating speed and the desired mileage in deflated condition was fixed at 45 mph and 50 miles, respectively.

The initial part of the design process for the auxiliary supported design involved using a rigid cylindrical structure of varying height and thickness as a rim-mounted run-flat insert to get estimate of life of tire structure for different levels of deformation. The results were then used as input for designing a deformable rim mounted insert using reinforced rubber material.

For the self-supported design, the sidewall of the tire was modified to increase its section thickness from an average value of 5 mm in the original design to 10 mm and 15 mm by addition of a hard rubber material. For each thickness value, three designs based on the location in the tire structure where the material addition began relative to the belt edges of the tire were created. The designs were compared in terms of their fatigue life and contact patch area.

For both types of run-flat designs, a candidate design, which satisfied the performance criteria, was found using the simulation results for the tire and run-flat system. It was concluded that a simulation-based approach can be used to design innovative run-flat systems for pneumatic tires.

Design and Analysis of an Innovative run-flat system for pneumatic tires

Abhishek Saraswat

GENERAL AUDIENCE ABSTRACT

Pneumatic tires have been an essential part of the automobile since the early 20th century. Providing load carrying, braking, accelerating and turning capability as well as a certain degree isolation from the road, they fail to function without the presence of air pressure inside them. Run-flat tire systems allow the vehicle to continue running with reduced driving speeds for a certain specified range in case of loss of air pressure due to puncture or damage. In this work, the design of self-supporting and insert supported run-flat systems was approached using computer aided design and simulation methods.

Two tire models of 14-inch and 18-inch wheel sizes were used in this study and distance travelled before failure when running in deflated condition was used as the primary parameter for design evaluation. Ride comfort and handling characteristics are important performance parameters for a tire. Thus, a limited study to quantify the effect of run-flat system on the ride and handling properties was also conducted. The maximum operating speed and the desired mileage in deflated condition was fixed as design targets at 45 mph and 50 miles, respectively.

For both types of run-flat designs, a candidate design, which satisfied the performance criteria, was found using the simulation results for the tire and run-flat system. It was concluded that a simulation-based approach can be used to design innovative run-flat systems for pneumatic tire

List of Contents

List of Figures

List of Tables

1 Introduction

1.1 The pneumatic tire

Pneumatic or air-filled tires are used in different modes of conveyance from bicycles to passenger vehicles, trucks and buses, and farming and heavy industrial equipment. Tires are the only component of a vehicle that are in direct contact with the road and provide load carrying, braking, accelerating and turning capability to the vehicle. The pressure of air filled inside these tires helps in supporting the load on the tire while also providing a cushioning effect from driving surfaces, bumps and potholes. The story of rubber tires starts with the invention of rubber vulcanization process by Charles Goodyear in 1839. Robert Thomson first patented the air-filled tire in 1845 but the idea did not pick up until 1888 when John Boyd Dunlop obtaining the patent for a air-filled bicycle tire. The majority of the tires used currently in passenger cars are radial tires where the cord plies run radially across the tire structure. Although the radial tire designs were patented earlier, it was designed, patented and commercialized in the form of Michelin X in 1946 which was a radial tire to be used in passenger cars.

Today, the global automotive tire market size stands close to 140 billion USD. Modern day pneumatic rubber tires have come a long way in terms of high performing designs and materials, but the basic structure remains the same. The structure of a passenger car radial tire is shown in Figure 1.1. The detailed discussion on tire construction and functions of individual components can be found in [1][2][3] with the functions of various components briefly described below:

(1) Bead - The bead or bead bundles are rings of steel wire which lock the tire to the rim and provide an anchor to the body ply of the tire.

(2) Bead Filler/Apex – It is usually the stiffest rubber compound used in a tire. It helps in providing good handling properties to the tire and has good adhesion properties with bead wires and ply compounds.

(3) Sidewall – This component covers the body plies from the sides of the tire. It provides protection from impact damage, abrasion and weathering. As this component flexes the most in normal running conditions, the rubber compound used in this region is made to be resistant to cracking due fatigue.

(4) Body Ply – Usually made up of polyester or nylon calendered within a rubber layer. Extending from bead to bead, it is the primary reinforcing component in a tire and provides structure to the tire and strength to contain the air pressure.

(5) Belts - Two layers of steel wires at opposing angles make up the belt component. They provide rigidity and stability to the tread region, and contribute to stability and handling, wear, and traction performance of the tire. They also provide a layer of protection to the body ply.

(6) Tread – This is the only component of a tire that comes in contact with the road surface in normal running condition. The performance parameters like handling and traction, fuel economy and wear are influenced by this component.

(7) Inner liner – This component is used to retain the inflation pressure inside a tubeless tire. This component covers the whole inner surface of the tire and is made up of low-permeability rubber compound.

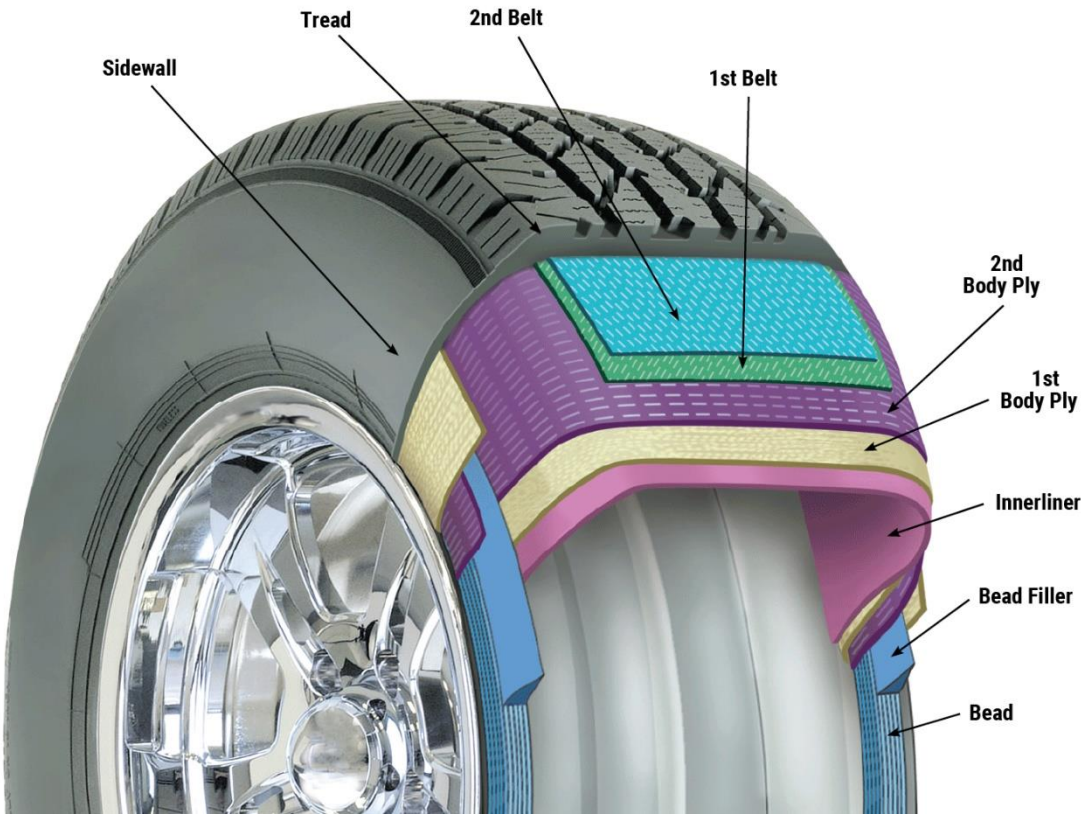

Figure 1.1 What's in a tire, used under fair use [4]

1.2 Run-flat tire systems

Tire blowouts pose significant safety risks causing instantaneous pressure loss, collapsing the sidewall and destabilizing the vehicle. Run-flat tires have emerged as a solution offering vehicle safety and reliability by maintaining vehicle control even under deflated conditions. Run-flat tires or systems allow the vehicle to continue running with reduced driving speeds for a certain specified range in case of loss of air pressure in tire due to puncture or damage. This thesis provides a simulation-based methodology for design and analysis of run-flat tire systems. Moreover, the thesis explores the challenges and limitations associated with run-flat tires, including effects on ride comfort and handling characteristics. Major portion of load on a pneumatic tire is supported by tension in the tire plies which appears due to the air pressure inside the tire. The tire structure by itself does not have the structural stiffness required to support vehicle load and it collapses when the

tire loses pressure. To provide load bearing capacity to a deflated tire, two types of run-flat systems are broadly used:

(1) Rim mounted support ring insert run-flat systems:

These systems are attached to the wheel of the tire in the form of a ring like insert. In case of pressure loss, the tire structure deforms and comes into contact with the insert which supports the tire load. The insert can be connected to the tire rim through different mechanisms and can be made up of a single piece or multiple pieces. An example of a single piece system is the Michelin Pax system [5]. These types of systems are usually heavier, require custom equipment to install and maintain and require a customized rim designed to mount the insert. The advantages offered by these systems is the ability to support much higher loads and no effect on ride quality in normal inflated running conditions. These types of run-flat designs would be referred to as insert supported run-flat (ISR) designs.

(2) Tire structure integrated self-supporting run-flat systems:

These systems are part of the tire structure. In these designs the sidewall of the tire is reinforced with added rubber material or insert. The stiffer sidewall supports the load on the tire without collapsing completely. These types of run-flat systems are easier to install and maintain and fit on regular rims. The disadvantages of these systems are a harsher ride quality and higher rolling resistance. These designs are also limited in terms of the levels of loads that they can support and are not suited for heavier loads as experienced by truck and bus tires. These types of run-flat designs would be referred to as self-supporting run-flat (SSR) designs.

The basic geometry of the two types of run-flat systems is show as a section an image in Figure 1.2 along with their individual advantages and disadvantages summarized in Table 1.1.

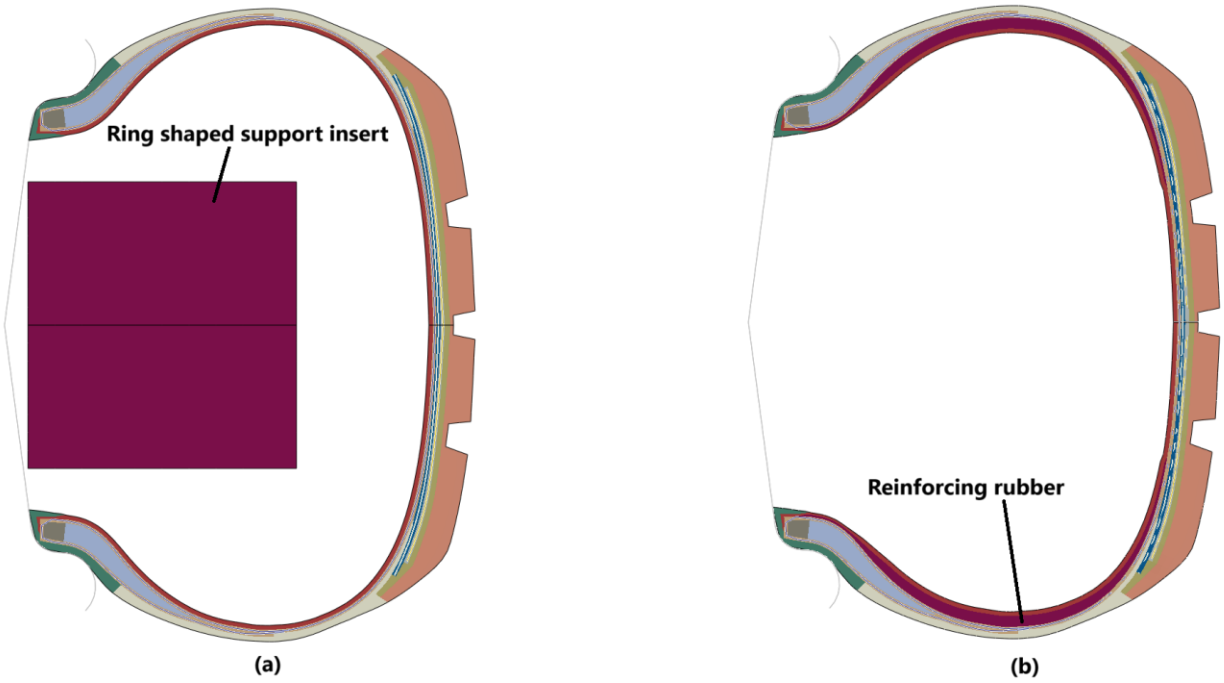

Figure 1.2 Types of run-flat system designs (a) Insert supported run-flat (ISR) (b) Self-supporting run-flat (SSR)

Table 1.1 Advantages and disadvantages of the two types of run-flat systems

Type	Advantages	Disadvantages
Insert supported system (ISR)	▪ Can be designed to work with higher loads ▪ Doesn't affect ride quality in inflated condition	▪ Custom rim designs may be required ▪ Specialized equipment required to install and maintain ▪ Generally heavier than the self-supporting designs
Self-supporting system (SSR)	▪ Design works with standard rims ▪ Easier to install and maintain	▪ Harsher ride and higher noise levels ▪ Not suitable for higher loads like truck tires ▪ Higher rolling resistance

1.3 Problem Statement and Contribution

Traditional pneumatic tires pose a significant safety risk in case of sudden air pressure loss due to punctures or blowouts which can lead to loss of vehicle control, accidents, and costly roadside assistance. Run-flat tires and systems are designed to offer reduced functionality after air pressure loss but, the current designs often compromise on the ride comfort, handling performance, durability, and fuel efficiency due to added weight and stiffness. This work aims to address these limitations by developing innovative designs and a CAE based design process for run-flat systems for tires that ensure safety, ride quality, and fuel efficiency, while minimizing trade-offs present in current designs.

(1) The traditional insert supported systems available commercially have a solid stiff ring like supporting insert. This design provides run-flat capabilities but adds a lot of weight to the system and provides due to very high stiffness of the structure, provides poor ride quality when running in deflated conditions. In this work, a deformable hollow structure is proposed as a potential design for the run-flat system which adds lesser weight and due to a relatively less stiff structure, offers better ride quality in deflated running condition.

(2) For the self-supporting system, a design strategy based on efficiently stiffening the tire structure in regions where higher deformations due to lower stiffness are observed in deflated conditions has been developed. This strategy saves computational time compared to using an uninformed design optimization process.

(3) A simulation-based approach is proposed to design run-flat systems for tires which saves a lot of cost from early prototyping and design process. Structural simulation of high deformations as is observed in run-flat tires is difficult due to multiple convergence issues in the simulation. Methodology to tackle such issues was developed using available processes in ABAQUS software. Endurica, which is a software tool for polymer fatigue analysis and incorporates the additional parameters unique to rubber fatigue analysis was used to ensure accurate prediction of fatigue life.

(4) Lateral force generation and ride quality are not discussed widely in available literature as part of the performance parameters of a run-flat system. These parameters are an important part of the overall performance of the system and are discussed in this work.

1.4 Thesis Structure

This thesis is organized into 9 chapters:

Chapter 1 - Provides an introduction to pneumatic tires and the run-flat tire concept along with the problem statement and contributions.

Chapter 2 - Contains the literature review of run-flat tire designs and fatigue analysis of rubber.

Chapter 3 - The theory of rubber fatigue and heat generation modeling in rubber as implemented in Endurica software is discussed.

Chapter 4 - The process of modeling and scaling a tire model, including modeling of mechanical and thermal properties of the components.

Chapter 5 - The design and modeling methodology for the rim-mounted and self-supporting type run-flat systems is discussed followed by methodology for structural, thermal, fatigue, and freerolling and lateral force generation simulations.

Chapter 6 - Includes the results from the simulations and design process. First, the fatigue thermal results for a base non run-flat tire are discussed followed by the results for the rim-mounted and self-supported run-flat designs.

Chapter 7 - Conclusions and future work.

Chapter 8 and 9 - References and Appendix sections respectively.

2 Literature Review

2.1 Run-flat tire system design

The self-supporting run-flat tire design was first proposed by Alden of BF Goodrich in 1977 [6] with a goal of eliminating the spare tire. Multiple support designs were tested in the design process including a rubber bead insert and a steel insert. The design with a load bearing strengthened sidewall was selected as the final design and was able to achieve a range of 45 miles in deflated condition at a speed of 45 mph. An overall weight saving was also reported considering the new design would lead to the removal of the spare tire and wheel.

Pannikottu et al [7] designed a type of self-supported tire for military applications with carbon fiber hoops embedded in rubber running across the circumference of the tire between the tire grooves and belts. In such a design, the tire load would be supported by ply tension in inflated condition and by the carbon fiber hoops in tension in deflated condition. The load-deflection curves for the reinforced tire in deflated tire were shown to be similar to those for a normal tire at 25 psi pressure. Although the load-deflection curves also showed that the stiffness of the reinforced tire with 20 psi inflation pressure was equivalent to that of a normal tire at 80 psi pressure. The durability of such a design was not discussed.

Liu et al [8] optimized the design of a self-supported run flat tire with two insert structures and 4 compounds to test a total of 6 designs. The designs were evaluated based on parameters like maximum stress of tire structure, maximum stress at apex and insert and strain energy density at apex and insert. The best design using these criteria was found to be the best design after durability testing on the physical tires.

Cho et al [9] used modulus of the insert rubber and maximum thickness of insert rubber as design parameters to optimize design of a self-supported run flat tire. Genetic algorithm-based optimizer was used to minimize the peak strain energy density at the insert for tire

fatigue life and minimize spring rate of the tire for ride comfort using ANN model of the tire. The final selected designs were simulated using FE models to verify the results.

Arndt [10] compared the vehicle handling characteristics with a temporary use spare tire vs a run-flat tire in deflated condition. Houben [11] in a limited study compared the ride comfort with an inflated normal and self-supporting run-flat tire using a half car model and found no difference in the comfort index between the two. For most tested tires the contact patch area and shape were also found to be similar.

Gardetto [12] has described a quick change high load insert supported run-flat design developed for use in a HMMWV vehicle made up of three load bearing cylindrical segments mounted to a torque ring using bolts. The torque ring is further bolted to the wheel using bolts. An elastomeric high strength formulated polymer material was used for the insert to increase the ballistic resistance. The height of the insert was selected to limit the deformation of tire in deflated condition to safe levels. On testing the design using a dynamometer in deflated condition at 30 mph, the test was stopped due to the tread separating from tire after 6 miles of test distance. In a later work, Gardetto et al [13] used a similar run-flat insert design mounted with a 37x12.5 R16.5 LT Goodyear wrangler. The tire failed at 28 min into the test with the tire temperatures reaching 330° F temperature in the shoulder region.

Liguo Zang and his co-authors have done a variety of work in the field of insert supported run-flat designs. Zang et al [14] optimized the design of a cylindrical run-flat insert for heat dissipation by introducing grooves in the surface. In [15] , the contact patch shape and stresses in the tire structure and the insert structure were studied. Topology optimization on a cylindrical three piece insert design to obtain 20% reduction in mass with a reduction in the factor of safety from 17.4 to 10.6 was performed in [16]. Wang et al [17][18] have discussed the effect on driving dynamics handling and stability of the vehicle with a insert supported run-flat system in case of a tire blowout.

Ejsmont et al [19] studied the rolling resistance values for a tire with insert supported run-flat system using test data. Up to 500% increase in the rolling resistance values was observed between inflated tire and fully deflated tire.

2.2 Fatigue life of rubber

The fatigue failure process involves two phases, first is the crack nucleation phase where the initially non existing crack becomes observable in the failure region and second phase is the crack growth phase where the nucleated crack grows till the point of failure. Two approaches are used for predicting fatigue life in rubber. One approach focuses on predicting crack nucleation life using stress and strain histories at a particular material point. The other approach focuses on predicting the growth of a particular crack with known geometry and energy release rate history of the crack. The review paper by Mars and Fatemi [20] provides a good comparison of the methods used for predicting fatigue life of rubber. It was concluded in the paper that the existing approaches fail when an established correlation using uniaxial testing is applied on biaxial testing data and a multiaxial nucleation life-based approach was required for accurate prediction of fatigue life of rubber.

These conclusions were followed by [21] in which three scalar equivalence criteria for multiaxial loading - maximum principal strain, strain energy density and cracking energy density were explored. The term cracking energy density (W_c) was first used by Mars in his PhD thesis [22] and is defined at a material point and for a specific failure plane by:

$$W_c = r^T . \boldsymbol{\sigma} . \boldsymbol{d}\epsilon . r$$

where,

r *is the unit vector normal to the plane being analysed*

$\boldsymbol{\sigma}$ *is the stress tensor at the material point and* $\boldsymbol{d}\epsilon$ *is the strain increment tensor*

Three criteria for selecting the failure plane were tested (1) The plane of maximum peak W_c in a loading cycle, (2) The plane of maximum peak ΔW_c in a loading cycle and (3) Plane with

minimum predicted fatigue life. The plane of minimum predicted fatigue life can be found by using values of W_c and ΔW_c for a preselected set of planes. It was found that the plane with minimum predicted fatigue life criteria gave the best correlation with test results. It should be noted that for uniaxial tension loading, the values of cracking energy density and strain energy density would be same for the failure plane. The cracking energy density criteria also accounts for the crack closing which occurs in compressive loading. The maximum principal strain criterion was found to be closest to the cracking energy density criterion in terms of fatigue life results.

For the second part [23], fatigue experiments were conducted with an axial-torsion specimen with combined torsion–compression, pure torsion, combined torsion– tension and pure axial tension which resulted in a broad fatigue life range of 10^3 to $2x10^6$ cycles. The equivalence criteria discussed above were then used to predict fatigue life. It was found that the maximum principal strain criterion gave the best correlation of fatigue life for the combined axial and shear loading while strain energy density gave the worst correlation. The cracking energy density criterion was found to give good correlation of fatigue life in the combined axial-torsion tests. It was also observed that because CED provides a plane-specific analysis, it was well suited for use in crack-nucleation based fatigue analysis when multiaxial strain histories are involved.

Some of the works that have use CED and SED based fatigue life analysis for rubber are listed below:

Barbash and Mars [24] used CED and critical plane analysis to predict fatigue life and failure mode of an automotive bushing under recorded road loads. The method was able to predict the fatigue life before failure and the location of failure after the same loads were applied on a test sample.

Kim et al [22] used CED and failure plane analysis for predicting failure of tires near the bead area. Paris law was used to model crack growth and the parameters for paris law were calibrated first using the known test results of tire life from a sample tire and the calibrated parameters were then used to successfully predict tire life for a different tire.

Nyaaba [25] used the CED and failure plane analysis approach to estimate the fatigue life of an ultra large mining tire. Thomas fatigue crack growth law was used with the rubber fatigue parameter estimation done using results from a static tearing energy experiment. The initial crack size was found using calibration from existing tire life test data. Strain induced crystallization of filled natural rubber and effect of loading R ratios were considered in the fatigue life prediction using Endurica CL fatigue solver. Optimal inflation pressure for different loading conditions was found using the method to get higher fatigue life.

Mars et al [26] used cracking energy density based critical plane analysis with incremental tire speeds to estimate fatigue life of a tire tested according to the FMVSS139 high speed testing standard. ABAQUS steady state transport capability was used to model the tire running at different speed along with Endurica DT as an incremental solver for fatigue life and for predicting residual life at each incremental speed step. This was used as the main reference for tire fatigue analysis in this work.

Liang et al [27] used the gradient of strain energy density as a parameter to predict life of TBR tires. The location of crack initiation as well as the direction of crack growth was predicted correctly for several test tires. A sensitivity study with the tire design was conducted and the width of belt 2 was found to be the most sensitive design parameter for cracks occurring in the shoulder region. A test tire constructed with design changes leading to improvement in fatigue life.

3 Rubber fatigue and tire structure heat generation analysis using Endurica software

In this work, Endurica software was used for computation of fatigue life of rubber and heat generation in the tire structure. Endurica is a validated fatigue life simulation software for elastomers which computes fatigue life and direction of crack growth based on the critical plane method and includes a rainflow counting algorithm to incorporate complex load cycles. Several models are available for modelling deviatoric and dilatational Hyperelasticity [28]. Various models including the Thomas power law model [29], Lake-Lindley model [30] [31] and custom table lookup method are available to model the crack growth rate vs peak crack driving force. The effect of non-fully relaxing load cycles (R ratio ≠ -1) and strain crystallization of rubber are incorporated using equivalent crack driving force modelled by Paris Model and Mars-Fatemi Model [32]. The heat generation is computed using power law model. This chapter discusses the theory behind fatigue crack growth and tire structure heat generation implemented in the software which is followed by a workflow for computing tire fatigue life using the software.

3.1 Crack growth rate and fatigue of rubber

The base assumption with which the fatigue growth is modelled is the presence of an initial small crack in all materials which is not observable due to the small size. This initial crack grows with every load cycle and finally reaches a 'final crack size' at which point the crack is said to be nucleated and the component is considered to have failed.

The number of loading cycles before failure N_f can be found by the expression

$$N_f = \int_{c_0}^{c_f} \frac{1}{f(T(c,t))}\, dc$$

where,

c_0 is the effective diameter of the preexisting idealized penny shaped crack in the material

c_f is the crack diameter at crack nucleation

f(T) defines the crack growth per loading cycle

The crack driving force 'T' is a linear function of the size of crack for sufficiently small crack lengths and is defined by:

$$T = 2\pi W_c c$$

Here, W_c quantifies the amount of strain energy that is available to be released as the crack grows. W_c is equal to the strain energy density for uniaxial and small strain loads. Endurica computes the value of W_c for different assumed failure planes termed as critical planes with assuming directions of crack growth. The such computed values are termed cracking energy density [22].

The Thomas power law model was used in this work to model the crack growth rate f(T) of rubber components. This model is based on the results from the 1959 paper by Thomas [29] where the experimental crack growth rate was found to be proportional to the square of tearing energy.

The Thomas power law defines the rate of crack growth by:

$$\frac{dc}{dN} = \begin{cases} r_c \left(\frac{T_{max}}{T_c}\right)^F \ for\ T \leq T_c \\ \infty\ for\ T > T_c \end{cases}$$

Here T_{max} is the maximum crack driving force observed in a given load cycle in a critical plane and T_c is the critical crack driving force. The crack growth rate for $T_{max} \leq T$ follows a power law function the slope of which is given by 'F' while the crack growth rate for $T_{max} > T_c$ is considered to be infinite which implies the material will fail for values of T_{max} greater than T_c. This model was used because of its simplicity and availability of material properties with the major drawback being that it does not provide a threshold value below which there would be no crack growth.

3.2 Heat generation in tires

3.2.1 Micro-kinematic framework

Endurica uses a micro-kinematic framework for computing energy dissipation is a hysteretic material. The energy dissipation in a material is a result of the dynamic deformation of the material which can be modelled as material lines or material planes. The deformation gradient as a function of time **F**(t) is used to capture the deformation cycle.

A material line defined by $\vec{\boldsymbol{R}}$ in the undeformed condition is represented by $\vec{\boldsymbol{r}}$ in the deformed condition. The deformed material line can be specified in terms of the undeformed material line and the deformation gradient by $\vec{\boldsymbol{r}}(t) = \boldsymbol{F}(t)\vec{\boldsymbol{R}}$. If the $\vec{\boldsymbol{R}}$ is assumed to be the normal vector of a material plane, the normal vector of the plane in deformed condition $\vec{\boldsymbol{s}}$ is given by $\vec{\boldsymbol{s}}(t) = \vec{\boldsymbol{R}}\boldsymbol{F}^{-\mathbf{1}}(t)$. The angle(ɣ) between the material line ($\vec{\boldsymbol{r}}$) and normal vector to the material plane ($\vec{\boldsymbol{s}}$) quantifies the shearing of the material plane.

In the heat generation model, the dissipation per unit of solid angle is assumed to be a function of the amplitude of the material line length and/or of the material plane shearing angle. The total volumetric energy dissipation H can therefore be computed by integrating contributions from each material fiber and/or each material plane across all possible orientations. The orientation of each fiber or plane is specified by the angles θ and ϕ. For all θ and ϕ the deformation history in terms of **r**(t) and **s**(t) can be counted to create a set of **K** constant amplitude elongation steps and **M** constant amplitude plane shearing events with amplitude $\Delta\mathbf{r}_k$ and $\Delta\mathbf{s}_m$. The material dissipation functions g($\Delta\mathbf{r}_k$) and h($\Delta\mathbf{s}_m$) define the hysteresis per unit solid angle as a function of strain amplitude. The total hysteresis in a loading cycle is then given by:

$$H = C\int\left((1-\chi)\sum_{k=1}^{K} g\left(\Delta r_k\left(\varepsilon_{ij}(t),\theta,\phi\right)\right) + \chi\sum_{m=1}^{M} h\left(\Delta s_m\left(\varepsilon_{ij}(t),\theta,\phi\right)\right)\right)d\theta d\phi$$

$where\ \chi\ specifies\ the\ degree\ of\ dependence\ of\ hysteresis\ on\ fiber\ elongation\ (\chi = 0)\ and\ material\ plane\ shearing\ (\chi = 1)$

$C\ is\ a\ scaling\ factor\ dependent\ on\ the\ mode\ of\ testing\ used\ to\ calibrate\ the\ material\ model$

The quantity 'H' gives the heat dissipated per unit volume for one loading cycle. If the time for one loading cycle is Δt, the power per unit volume $\dot{q}$ can be calculated by $\dot{q} = \frac{H}{\Delta t}$

3.2.2 Power law dissipation function

The power law dissipation models for functions g(Δ**r**) and h(Δ**s**) specify the relationship between the direction-specific strain amplitude Δ**r**/2 (for a material fiber) and the shear strain amplitude Δ**s**/2 (for a material plane) and the hysteresis per unit of solid angle. In this work only the shear strain amplitude is used for hysteresis calculation which is given by:

$$h = h_0 \left(\frac{\Delta s/2}{\epsilon_{a,0}} \right)^{\gamma} e^{r(\theta - \theta_0) + Z(\dot{\epsilon} - \dot{\epsilon_0})}$$

$h_0\ is\ the\ reference\ value\ of\ hysteresis\ occuring\ for\ a\ reference\ strain\ amplitude\ of\ \epsilon_{a,0}$

$\gamma\ is\ the\ powerlaw\ slope\ for\ the\ hysteresis\ function$

$r\ specifies\ the\ temperature\ dependence\ of\ hysteresis\ function\ relative\ to\ reference\ temperature\ \theta$

$Z\ specifies\ the\ strain\ rate\ dependence\ of\ hysteresis\ function\ relative\ to\ reference\ rate\ \dot{\epsilon_0}$

3.3 Workflow for fatigue life calculation of a tire using Endurica

Figure 3.1 shows the workflow for computing fatigue life using Endurica. The process starts with the export of engineering strain results from the last step of ABAQUS structural simulation, using a Python script. The data for all elements is stored in a database format compatible with Endurica software. Due to the circular symmetry of tires, the structural results inherently contain the full load cycle of each element i.e. every element in the ring of elements shown in the figure goes through the same stress-strain cycle in one rotation of the tire. This property is utilized by specifying the number of elements in one sector of the

3D tire model. Using the total number of elements in the model, the number of sectors is calculated. The crack energy density for each element in the ring across the tire is computed for a predefined number of planes. These CED values across the deformed circular ring of elements is equivalent to the CED variation data of one loading cycle for a single element in the 2D axi-symmetric section. All elements are processed using the same 'ring of elements' approach.

The hysteresis properties of rubber material are temperature dependent. For this reason, heat generation and temperature profile simulations are executed in an iterative way. The strain data from the element rings along with hysteresis parameters computed at the specified starting temperature are used to compute heat generation per unit volume in a single rotation of tire for each element in the 2D axi-symmetric model. The undeformed volume of the ring is then used to compute the total heat generated. The period of rotation of the tire is used to convert this value to power and heat flux. The procedure to get accurate period of rotation is discussed in 5.2.2. This heat flux is used as input to the thermal simulation of the axi-symmetric model. The details of thermal simulation procedure in ABAQUS are discussed in 5.2.3. After the first set of temperature values across the tire section are extracted from the thermal simulation results, the hysteresis properties for each element are updated for the current temperature which is followed by heat flux calculations with the updated hysteresis properties. This process is iterated till the temperature variations between iterations reach a specified error value.

After the steady state temperature is achieved in thermal simulation, Endurica computes the fatigue properties for each element using the final temperature from thermal simulation and temperature dependence of the critical crack driving force specified in material properties. These properties along with the CED data computed earlier are then used to predict fatigue life of each element of the tire cross section. The fatigue life is predicted in number of cycles before failure which is used to calculate the distance covered by the tire.

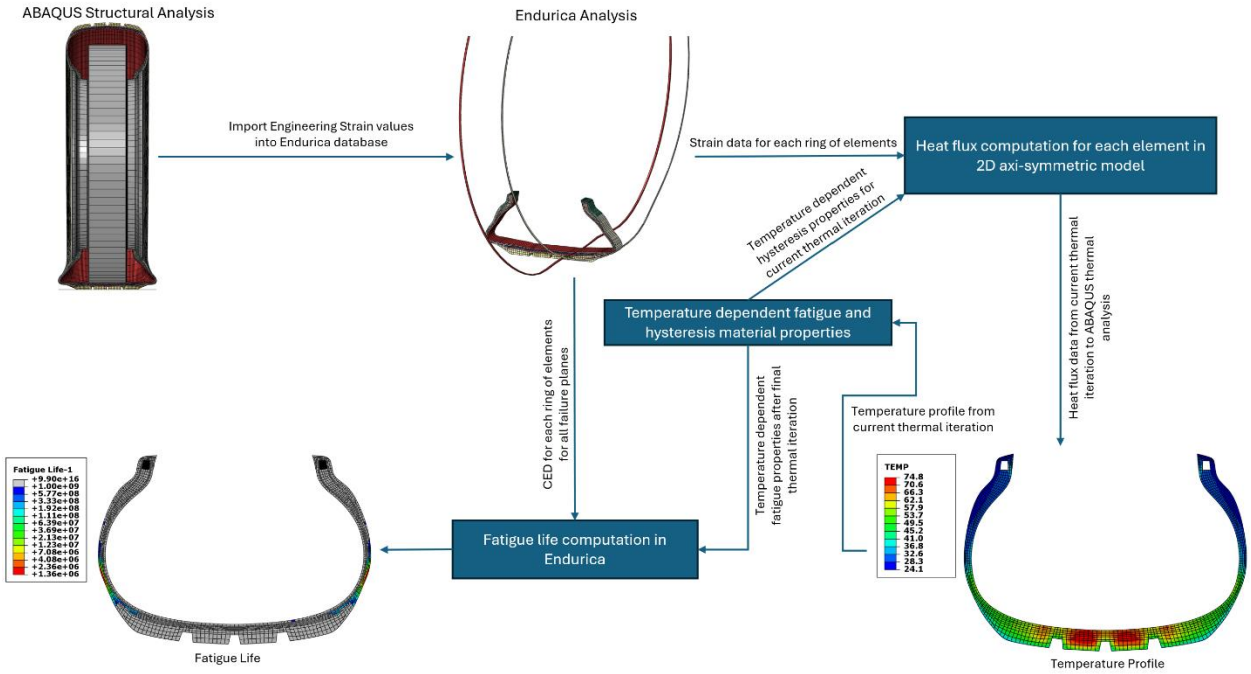

Figure 3.1 Workflow for fatigue life calculation using Endurica

4 Modelling

This chapter deals with the modelling of tire and run-flat system and modelling of mechanical, thermal, hysteresis and fatigue properties of tire components.

4.1 Tire modelling

The modeling of tires starts from a 2-D layout with different sections signifying different rubber components and reinforcements. Figure 4.1 shows the modelled components of the tire used in this work.

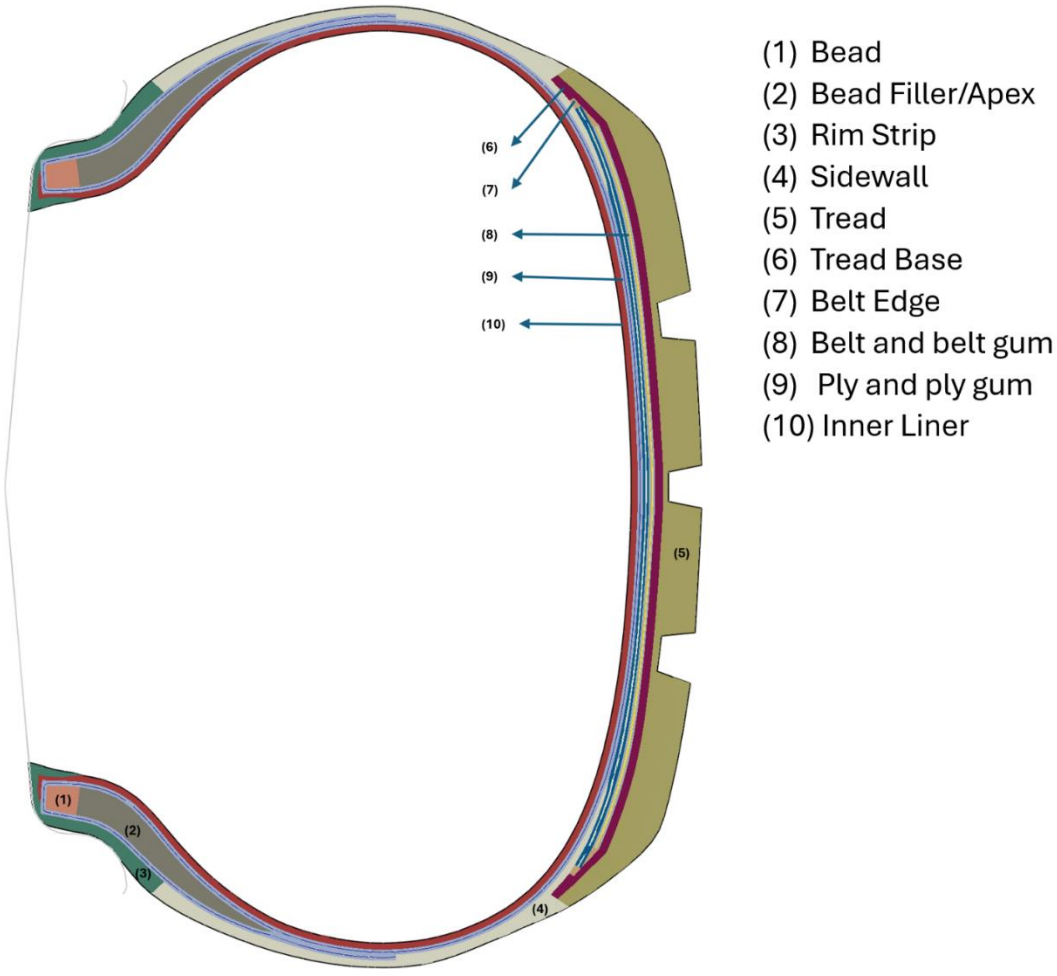

Figure 4.1 Tire model and components

The FE tire model of size 175/70 R14 from a previous study [33] was used in this work with certain modifications. The existing mesh was refined to a finer mesh with an average

element size of 2.5 mm. A fine mesh was required to capture the variations in strain energy density in the critical regions where the probability of the tire failing was high. The fatigue material properties of each component of tire are different and thus it was necessary to add components to the existing model to bring it closer to the structure of an actual tire. For this, two additional components - tread base and belt edge were introduced in the existing model. The geometry of the tire and ply-lines were preserved when adding new components.

Belt Edge - For normal loading and inflation conditions, the edges of the steel belt show high value of strain energy density and are the most common point of failure of a tire. To decrease the failure risk, tire belt edges are wrapped with the belt gum compound that helps in decrease of SED and enhances the life of tire.

Tread Base - Although the same mechanical properties are used for tread base and belt gum, the fatigue properties of tread base component are usually different from that of the belt gum. So, a new component of tread base was added to the model.

The thickness of different rubber components in the model is listed in Table 4.1.

Table 4.1 Thickness of rubber components in tire model

Component	**Thickness (mm)**
Inner Liner	1.2
Ply	1
Belt	1
Tread Base	1.5
Tread	7.5
Sidewall	1.5 - 3

The FE modelling was done in ABAQUS with the rubber components modelled using CGAX3H and CGAX4H axisymmetric element types for tri and quad elements respectively. The axisymmetric elements with twist were used for capturing the effects of out of plane

stiffness in the model. The hybrid formulation was used for accurate analysis of rubber components considering their in-compressibility with Poisson's ratio being close to 0.5. Elements of type SFMGAX1 were used to model the belt and ply reinforcements. These elements were specified to be embedded in the rubber elements as rebar elements.

4.2 Tire model scaling

To ensure the run-flat designs and design processes are robust and would work for a variety of tires, it was required that the design process be applied to different tire sizes. Availability of tire model of only one size necessitated the need of scaling the tire model to different size. For this work, the existing tire FE model of size 175/0 R14 was scaled to 175/60 R18. Although the tire design process does not allow direct scaling of tire models, keeping the nominal width of the tire equal for both sizes made the scaling process acceptable. Scaling the model to get the new section height followed by an offset of the whole model to incorporate larger rim size was used to create the new size model. A MATLAB code was written to automate the scaling process (9.1). The ETRTO (European Tyre & Rim Technical Organisation) standards manual [34] provides guidelines for the dimensions of different tire sizes as listed in Table 4.2. The dimensions specified are for an inflated tire mounted on the recommended rim size. Table 4.3 lists the actual dimensions of the FE models mounted on the recommended rim and inflated to the specified pressure.

The different tire sizes required different rim sizes with the 14-inch tire requiring a 5JX14 size rim and the 18-inch tire requiring a 5JX18 size rim. The rims were created in AutoCAD using specification from ETRTO engineering design handbook [35] and converted to ABAQUS analytical geometry for use in simulations along with the tire models.

Table 4.2 Tire dimensions according to the ETRTO standards manual

Tire Size	Rim Size	Section Width (mm)	Overall Diameter (mm)	Load Capacity (kg)	Inflation Pressure (kPa)
175/70 R14	5JX14	177	602	500	250
175/60 R18	5JX18	177	667	515	250

Table 4.3 Dimensions of the mounted and inflated tire FE models

Tire Size	Design Section Width (mm)	Overall Diameter (mm)
175/70 R14	177.0	602.7
175/60 R18	177.3	674.9

4.3 Material Modeling and Properties

4.3.1 Mechanical and thermal properties

Rubber and other polymers can withstand high levels of strains, and the material modelling must consider finite strains. The finite strain formulation starts with defining the deformation tensor **F** for a material point at **x** and with reference at **X** as $\boldsymbol{F} = \frac{\delta \boldsymbol{x}}{\delta \boldsymbol{X}}$

The total volume change at the point is given by $J = \det(\boldsymbol{F})$

$Only\ deviatoric\ deformation\ gradient\ \overline{\boldsymbol{F}} = J^{-1/3}\boldsymbol{F}$

$The\ deviatoric\ strech\ matrix\ can\ be\ defined\ as\ \overline{\boldsymbol{B}} = \overline{\boldsymbol{F}}\overline{\boldsymbol{F}}^{T}$

$The\ first\ deviatoric\ strain\ invariant\ is\ then\ given\ by\ \overline{I_1} = \overline{\lambda_1}^2 + \overline{\lambda_2}^2 + \overline{\lambda_3}^2 = trace(\overline{\boldsymbol{B}})$

$where\ \overline{\lambda_i}\ are\ the\ deviatoric\ principal\ stretch\ ratios\ given\ by\ \overline{\lambda_i} = J^{-1/3}\lambda_i$

Hyperelastic materials properties are modelled in terms of strain energy potential which is the strain energy stored in the material per unit volume in reference state as a function of

strain at that material point. Amongst the different strain energy potentials available in ABAQUS software [36] for modelling approximately incompressible isotropic elastomers, in this work the Neo-Hookean form of strain energy potential was used. The Neo-Hookean model is not able to capture the upturn in the stiffness of rubber as is usually observed in the test data, but the values of maximum strain found from simulation was less than 50% and all material models are able to predict stresses accurately for this strain range as has been show in the ABAQUS benchmarks manual [37].

The Neo-Hookean form of strain energy potential is defined by:

$$U = C_{10}(\overline{I_1} - 3) + \frac{1}{D_1}(J^{el} - 1)^2$$

where,

$U\ is\ the\ strain\ energy\ potential\ and\ C_{10}\ and\ D_1\ are\ material\ parameters$

$J^{el}\ is\ the\ elastic\ volume\ ratio\ and\ \overline{I_1}\ is\ the\ first\ deviatoric\ strain\ invariant$

Using this formulation, the initial (small strain) values of shear modulus and bulk modulus are given by:

$$Shear\ Modulus\ (\mu) = 2C_{10}\ , K = \frac{2}{D_1}$$

The set of material properties used in [26] were used in this work and are listed in Table 4.4. The density of all rubber components was assumed to be 1100 kg/m^3. The thermal conductivity of all rubber components was assumed to be 0.25 W/mK. A linear elastic modulus was used to model the stiffness of steel bead and belts as well as the reinforcing ply as listed in Table 4.5.

Table 4.4 Mechanical properties of rubber components

Component	C_{10} (MPa)	D_1 (1/MPa)
Bead Filler/Apex	3.63	0.0028
Rim Strip/Abrasion	1.71	0.0059
Sidewall	1.79	0.0056
Tread	1.04	0.0096
Tread base	4.06	0.0025
Belt gum and belt edge	4.06	0.0025
Ply gum	1.79	0.0056
Inner Liner	0.64	0.0158

Table 4.5 Mechanical properties and configuration of reinforcement

Component	Modulus (GPa)	Density (kg/m^3)	Cross-section area (mm^2)	Distance between cords (mm)	Angle
Bead	135	7500	NA	NA	NA
Belt	76	7500	0.332	1.27	+- 22°
Ply	4.6	1300	0.385	1.27	0°

4.3.2 Fatigue and hysteresis properties

The following properties were used to model the fatigue of rubber components using Thomas power law to model fatigue crack growth rate.

(1) Initial crack size (c_0) – Defines the size of the preexisting crack in material. The fatigue life is highly dependent on this parameter, and it is estimated using calibration with test data.

(2) Final crack size (c_f) - The final crack size defines the crack size at which the component would be considered to have failed. The value was fixed to 1 mm for all components.

(3) Crack growth rate (r_c) – Defines the growth of crack in one cycle. The crack growth rate was fixed at 0.01 mm/cycle

(4) Slope of power law (F) – This factor defines the slope of the Thomas power law model used to compute crack growth rate. The value of F was 2.0 for all components.

(5) Critical value of crack driving force (T_c) – Specifies the value of the critical value of crack driving force used in Thomas power law model.

With the values and c_f, r_c and F fixed for all components, the values of c_0 and T_c for all rubber components used in the tire model are listed in Table 4.6. Although T_c was modelled as a temperature dependent parameter specified using tabular data, only the values at 25°C are listed in the table. As only one set of hysteresis properties was available the same properties were used for all components and are listed in

Table 4.7.

Table 4.6 Crack growth properties of rubber components

Component	**Initial crack size c_0 (mm)**	**Critical crack driving force Tc at 25° C (kJ/m²)**
Bead Filler/Apex	0.03	285
Rim Strip/Abrasion	0.001	285
Sidewall	0.005	16
Tread	0.1	20.75
Tread base	0.008	120
Belt gum and belt edge	0.01	120
Ply gum	0.01	285
Inner Liner	0.05	38.25

Table 4.7 Hysteresis properties of all rubber components

Parameter	**Value**
χ	1.0
γ	1.94
h_0	9500
Z	0.3
$\dot{\varepsilon_0}$	2.0
C	2.66
ε_a	0.1
r	-0.0074
Θ_0	82

5 Methodology

5.1 Design Methodology

The methodology for designing rim mounted and self-supporting run-flat systems are discussed in this section.

5.1.1 Insert supported run-flat (ISR) systems

The design of insert supported run-flat systems involved a preliminary study of deformation and fatigue life of the tire structure for different insert heights and widths. The preliminary designs used a rigid cylindrical geometry of the support insert for studying the tire structure fatigue life at different levels of deformation. The rim geometry was modified to include the geometry of the run-flat inserts of width 60 mm and 80 mm with three heights of 0,75 and 80 mm as shown in Figure 5.1. A MATLAB code (9.2) was written to read the ABAQUS input files for the base rim geometry and modify it to include the different size inserts. The modified input files were again saved as ABAQUS input files.

The tire structure fatigue life results from the preliminary study were used to decide the final dimensions of a deformable cylindrical hollow insert of reinforced rubber of cross section thickness 5 mm and 10 mm. The structural and fatigue life simulations were repeated for the deformable insert to verify that the design goals are met.

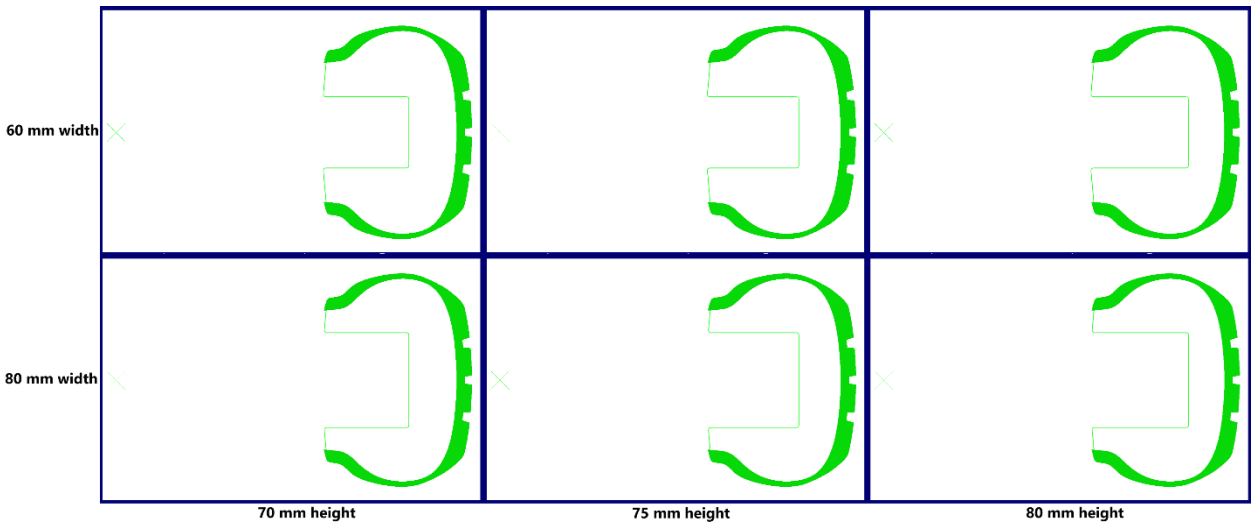

Figure 5.1 Rim geometry with integrated run-flat inserts

5.1.2 Self-supporting run-flat (SSR) systems

Self-supporting or zero pressure tires support the tire load in deflated condition by incorporating an additional layer of stiff rubber compound at the sidewall to using a strengthening the structure of the tire itself. The added component strengthens the sidewall and makes it load bearing. The design strategy for the self-supported design was to maintain a constant thickness for the tire section from belt edges to apex. Designs with section thickness of 10 mm and 15 mm were used.

Figure 5.2(a) show the designs developed for 10 mm and 15 mm section thickness. The 'center' designs start addition of reinforcing rubber component from the point where the total section thickness of tire is 10 or 15 mm respectively. The 'higher' and 'lower' designs shift the starting point by 6 mm towards or away from this point. For the 10 mm thickness design, the starting point of 'center' design coincided with the edge of lower belt while for the 15 mm thickness design, the starting point of 'lower' design coincided with the edge of upper belt. Figure 5.2(b) shows the belt edges and starting points of the rubber reinforcement layer. The belts edges were used as reference point as beyond these points, there is a sudden decrease in the tire structure stiffness. The addition of reinforcing layer leads to an increase in the mass of the tire. The total mass of each design is listed in Table 5.1. The total mass of the base tire is 7.81 kg with the total mass of rubber being 6 kg. The

15 mm thickness designs add more than 2 kg of mass to the tire which is 33% more rubber material than the base tire. This additional rubber would lead to higher heat generation and rolling resistance. After selecting the best design from the study for 14-inch tire, the process was repeated for the 18-inch scaled tire to verify the robustness of the design.

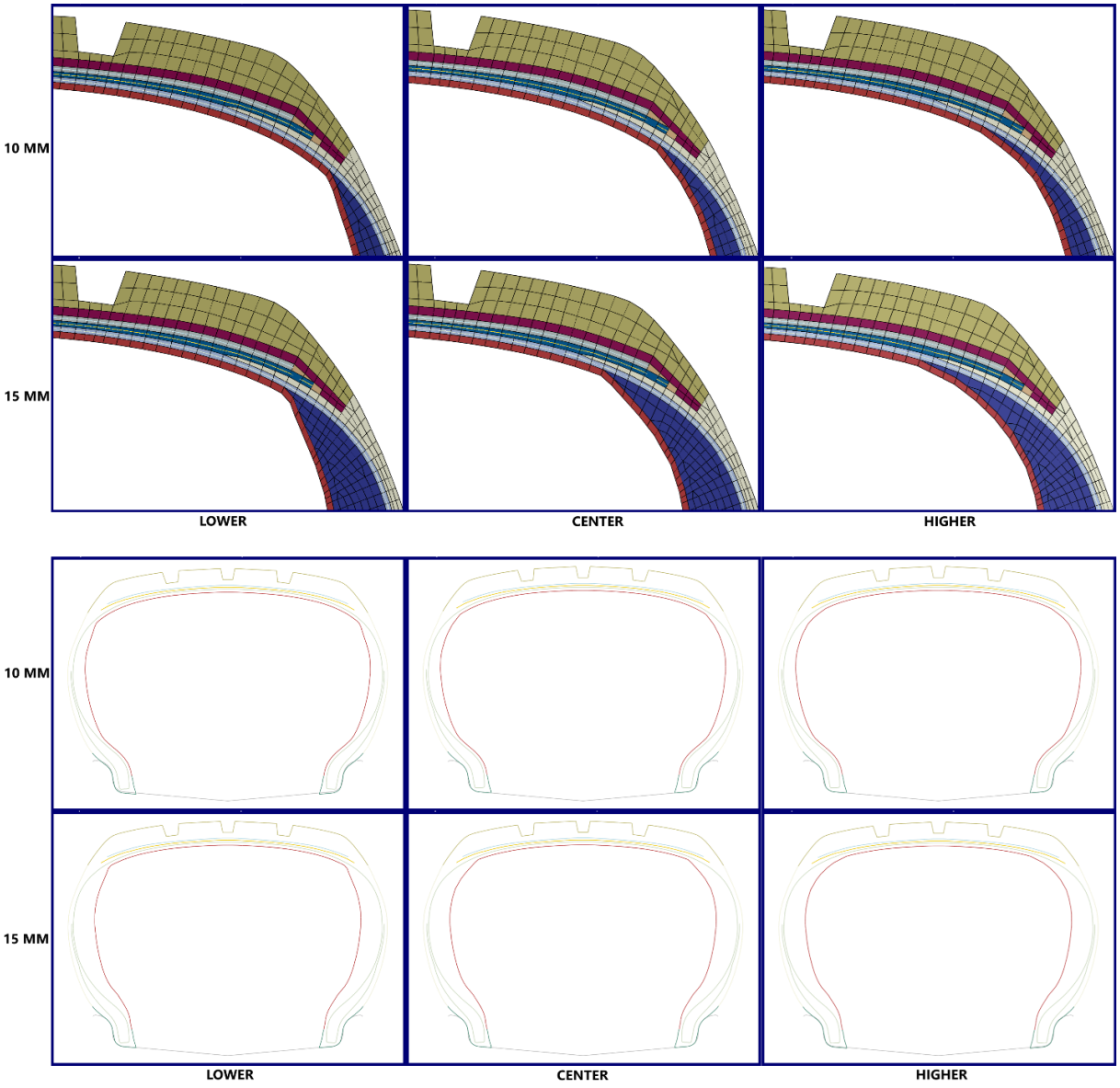

Figure 5.2 (a) Starting points for reinforcing rubber layer (b) Edges of tire structure belts and ply

Table 5.1 Total mass of 14-inch base and self -supported tire designs

Model	Mass (kg)	Added Mass (kg)
Base model	7.81	0.0
10 mm lower	8.64	0.83
10 mm center	8.68	0.87
10 mm higher	8.70	0.89
15 mm lower	9.92	2.11
15 mm center	10.02	2.21
15 mm higher	10.05	2.24

5.2 Simulation Methodology

In this section, methodologies implemented for the FE simulations employed in this work will be discussed.

5.2.1 Structural simulation methodology

The performance study of the run flat systems starts with the structural simulation. ABAQUS was used for structural simulation of the tire-run-flat system. Figure 5.3 shows the tire structural simulation workflow.

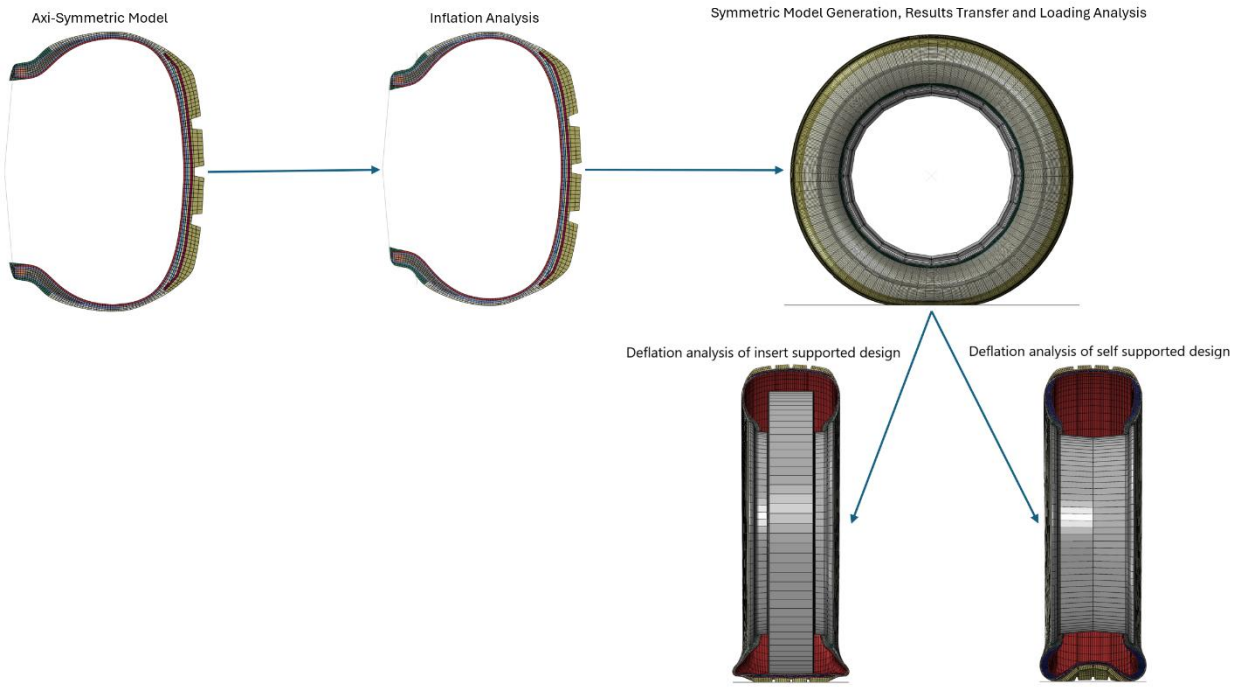

Figure 5.3 Structural simulation methodology for tire and run-flat system

The structural simulation of tire starts with the rim mounting and inflation analysis of the tire section taking advantage of the axi-symmetric nature of tire. The completion of inflation process in the axisymmetric model helps with saving computational time when moving to the full 3D model. After completion of the inflation analysis, symmetric model generation is used to create the full 3D mesh. In this step, CGAX3H and CGAX4H elements are converted into C3D6H and C3D8H elements respectively and the 2 node SFMGAX1 rod elements are converted into SFM3D4R type surface elements. After the model generation, results from

the axisymmetric analysis are transferred to the 3D model followed by an equilibrium analysis step.

The tire is then loaded first by moving the rim by a small distance such that the tire comes in contact with the road surface. Appropriate load from Table 4.2 are used to load the tire using a road surface which is defined as an analytical rigid body. After contact is established, loading force is applied to the rim reference node to complete the loading process. The final deflation step is completed by gradually reducing the pressure inside the tire in steps and finally removing the pressure altogether. The deflation of tire can be done in two ways (a) Loading the tire first and then decreasing the air pressure to zero in steps (b) Decreasing the pressure to zero after equilibrium step and then continue loading the tire skipping the loading step. Based on multiple trials, it was found that following the procedure (a) lead to lesser convergence issues and hence this method followed for all deflation analysis in this work.

Because of the angled steel belts, radial tires have an inherent structural anti-symmetry between the left and right sections which could have been used with correct boundary conditions to save computational time by simulating one half of the tire. It was observed in structural simulations with half tire that the grooves in the tire were deforming and crossing the symmetry plane. This would mean that due to higher deflections, the groove surfaces would come into contact in the full tire model. To ensure that the proper contact conditions are established, it was decided to use the full tire model for all simulations.

5.2.2 Rolling and cornering simulation

For computing heat generation (discussed in next section) in the tire, it is crucial to get an accurate value of the period of rotation of tire. For a given speed, the period depends on the free rolling angular velocity of the tire which can be calculated if the free rolling radius is known. An unloaded tire free rolling on a surface without slipping would have its rolling radius equal to the radius of the tire but that would not be true for a loaded tire. A loaded

tire can be said to be free rolling when there is no moment across the rim center required to keep the tire rolling. A moment has to be applied to the tire rim in order for the tire to be in a state of braking or traction and a tire rolling free would ideally not require any moment to be applied to the rim. In reality, the tire rubber being viscoelastic leads to dissipation of energy even for freerolling tire and hence a moment is required to maintain constant rolling speed.

For a free rolling object, the linear speed is given by the expression $v = \omega R$ where v is the linear speed, ω is the angular velocity and R is the rolling radius. For conditions where this expression is not satisfied, the object can be considered to be in a state of slipping. The slip ratio defined by $Slip\ Ratio\ (S) = \omega R/v$ indicates the slip state of the object with a slip ratio less than one denoting a braking condition and a slip ratio greater than one denoting a traction condition.

To compute the value of free rolling radius for a loaded tire and for further rolling simulations, the steady state transport analysis capability of ABAQUS was used [38][39]. The friction coefficient between tire and road surface was assumed to be 0.8 for all cases and a friction coefficient of 1.1 was used for rubber-to-rubber contact. Two angular velocities were chosen such that the moment observed at the rim where of opposite signs. Linear interpolation was then used along with multiple iterations to get the value of angular velocity where the moment at rim reaches a value close to zero. To help with convergence issues, inertia effects were not considered in the simulation. This angular velocity was then used to compute the free rolling radius. It is established that assuming the distance between rim center to the edge of the topmost belt usually gives a good approximation for the rolling radius which was found to be true when rolling analysis was done for the tires in this work.

For changing the direction of the vehicle motion from a straight line, cornering or lateral forces are required which are generated when the tire is steered in a particular direction. Steering input introduces a slip angle, and the angular velocity and linear velocity of the tire no longer remain orthogonal. As part of the design performance study, it was important to analyze the effect on lateral force generation when the tire is running in deflated condition.

To estimate the lateral forces generated when the tire is rolling with a slip angle in simulation, the linear velocity of the tire was assumed to be at an angle (equal to the slip angle) with the longitudinal direction and the components of the velocity in longitudinal and lateral direction were calculated. Table 5.2 lists the velocities in the longitudinal and lateral directions for different slip angles when the tire is rolling at a speed of 45 mph. These velocities were used in the rolling simulation to estimate the lateral forces generated at different slip angles for the tire.

Table 5.2 Longitudinal and lateral velocities for different slip angles for tire speed of 45 mph

Slip Angle (°)	Velocity in longitudinal direction (m/s)	Velocity in lateral direction (m/s)
0	20.11	0
1	20.107	0.351
2	20.098	0.702
3	20.082	1.052
4	20.061	1.403

5.2.3 Thermal simulation

Thermal simulation was required to get the temperature profile of the tire cross section as well as the insert. The material fatigue properties are highly dependent on the temperature which makes predicting the temperature profile of the structure essential for accurate prediction of fatigue life. The thermal analysis was done on an axi-symmetric model assuming the temperature would not vary in the circumferential direction. The same mesh as used in structural simulation was used by replacing CGAX3H and CGAX4H elements with axi-symmetric thermal elements of type DCAX3 and DCAX4 respectively. The elements representing steel bead and belts were removed as they have relatively higher thermal conductivity and show negligible hysteretic heat generation. The heat flux generated in the loading cycle of individual element of the axi-symmetric model is

computed by Endurica and is applied as heat flux boundary conditions to the 2D model. Heat transfer takes place from tire structure to the surroundings which include the air inside tire cavity, outer air and road. Due to the much higher heat capacities, all these are assumed to be constant temperature sink/source. The different heat transfer paths are:

(1) Inner surface to tire air cavity - Heat is transferred from inner liner to the air inside tire cavity. It can be assumed that the inside air moves at the velocity same as that of the surface and hence only a conduction coefficient was used. A film coefficient of 10 W/(m^2K) was used with a sink temperature of 40° C [26].
(2) Outer surface to environment - Heat is transferred to the environment from the outer surface of the tire. Due to the airflow around the tire, the heat transfer would be convective. A convective film coefficient of 83 W/(m^2K) computed for a speed of 20 m/s (45 mph) was used with a sink temperature of 23° C.
(3) Tire road interface - The heat is transferred by conduction for the tire-road interaction surface. Considering that only a fraction of the tread is in contact with road at any instance, the whole tire outer surface including tread is assumed to be transferring heat to the environment.

Figure 5.4 shows the inner and outer heat transfer surfaces of the tire.

The heat generated by each element in a rolling cycle is computed by Endurica using the viscoelastic material parameters. As the viscoelastic parameters themselves are dependent on the temperature of rubber, the thermal simulation is done in an iterative way. The thermal simulation is initialized by assuming the tire structure to be at a temperature of 25° C and heat generation is computed. After the thermal simulation is completed, heat generation is computed again by considering the effect of updated temperatures on the hysteresis properties. This process is repeated till the change in temperatures between iterations is below a selected value.

With the self-supported run-flat design, the heat transfer surfaces remain the same but for the rim supported run-flat design, additional surface of the insert are added which generated and transfer heat to air. The heat transfer coefficient and source/sink

temperature for the insert surfaces is kept the same as that of the tire inner surface. The heat conduction between the rim-mounted insert and the tire inner surface when they come in contact in deflated condition was not modelled in this work.

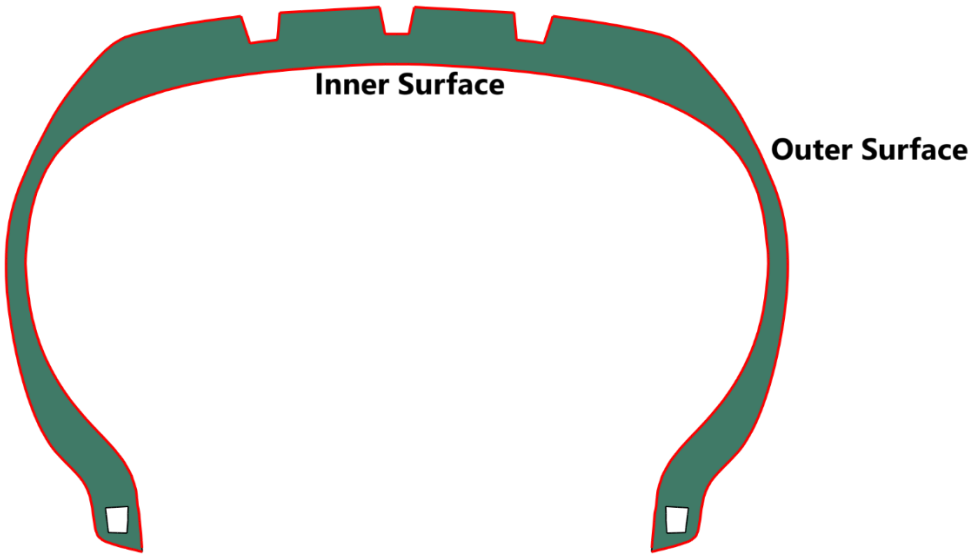

Figure 5.4 Heat transfer surfaces of tire

5.3 Design target and performance metric

The run-flat designs were analyzed based on the below performance parameters:

(1) Fatigue Life – This is the most important parameter as the design goal of this work is to achieve 50 miles or more of distance before failure at a maximum speed of 45 mph for the tire running in deflated condition with 100% rated load.

(2) Contact Patch – Contact area and contact pressure are important design criteria for tire handling and wear performance. Larger contact area generally helps in the stability of the tire while larger and concentrated contact pressure leads to higher and uneven wear. The contact patch shape and area along maximum contact pressure were used as a design performance metric.

(3) Handling and Ride – Lateral force generation in inflated and deflated conditions were compared for the designs. The operating point stiffness was used to judge the ride quality.

(4) Rolling Resistance – The rolling resistance value indicates the efficiency of the tire and is an important criterion more so if the system is being designed to the equipped in an electric vehicle. The predicted rolling resistance values for the designs were compared to the base designs to estimate the changes in energy efficiency of the tire compared to the base tire designs.

6 Results

6.1 Results for 14- and 18-inch base tires

This section includes the results of mesh size convergence study performed with the 14-inch base tire in terms of the number of sectors used in the creation of 3D tire model. Next, the structural thermal and fatigue life results for the base 14-inch tire model and the scaled 18-inch tire model are discussed. These results would establish a reference point for the later studies involving run-flat tire designs.

6.1.1 Mesh convergence study for structural simulations

The tire section is meshed with an average element size of 2.5 mm which is sufficiently small for our purpose and hence no convergence study was done for the section mesh. When this section mesh is revolved around the tire axis to create the 3D mesh, the element size along the circumference would vary with the number of sectors created. A convergence study for the 14- and 18-inch base tires was conducted based on the number of elements in the circumference i.e. the number of sectors with sector angles of 6,4 and 3 degrees which correspond to 60,90 and 120 sectors respectively. The study was done on the 14-inch tire model with inflation and 100% load. Strain energy density was chosen as the quantity to be studied as its convergence depends on convergence of both stress and strain values. As fatigue life was the major performance criteria for this work, fatigue and thermal simulation for the three sector angles was included as a part of the study.

Figure 6.1 shows the results for strain energy density for belt, ply and sidewall components for different number of sectors. The maximum SED values for each component are listed in Table 6.1(a). The % change in max SED for belt components is close to 4% for 4° sector size and less than 2% for other components. Results for the fatigue life and maximum temperature are listed in Table 6.1(b) and it was observed that the predicted fatigue life does not change when changing sector angle from 4° to 3° and there is very small change in the maximum temperature of the tire. Considering good levels of convergence of SED,

predicted fatigue life and temperature, the sector size of 4° was chosen for all structural simulations. Although a lower sector size could have been selected, decreasing the sector size further would lead to higher computational times. A reduced sector angle was however used for certain structural simulations where the simulation with 4° sector angle lead to convergence issues.

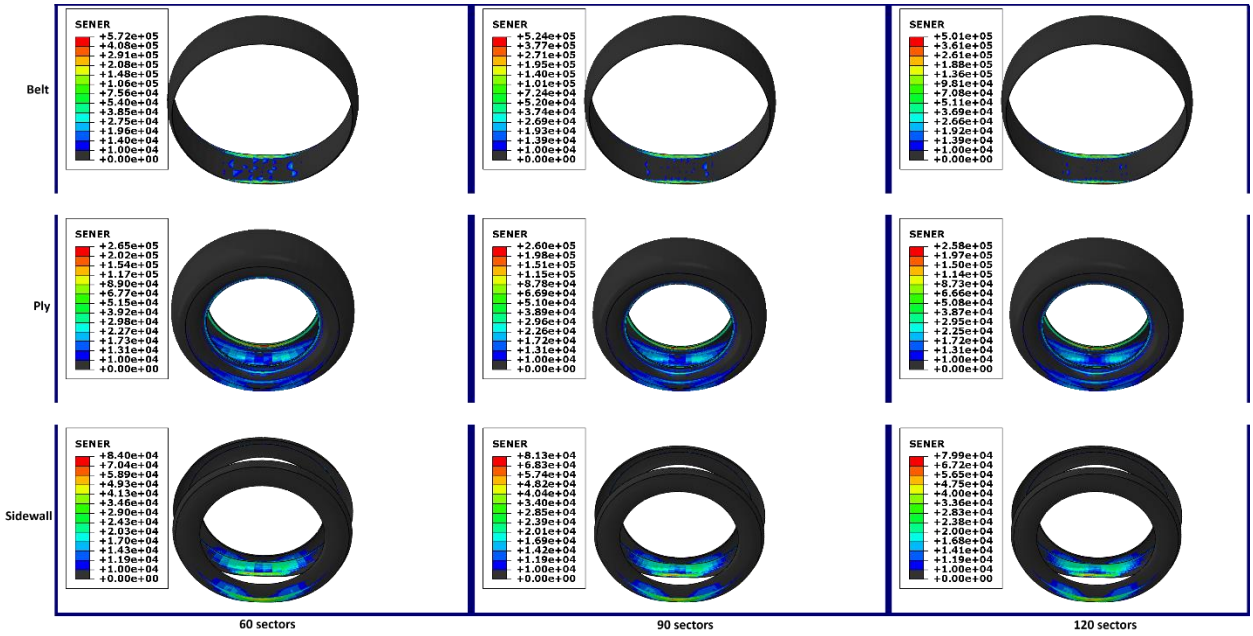

Figure 6.1 Strain Energy Density for different sector sizes for belt, ply and sidewall region

Table 6.1 Convergence study (a) Maximum SED (b) Vertical Deflection, life cycles and maximum tire temperature

		Maximum Strain Energy Density (J/m3)					
Sector Angle	No. of sectors	Belts	% Change	Ply	% Change	Sidewall	% Change
6	60	5.72E+05	NA	2.65E+05	NA	8.40E+04	NA
4	90	5.24E+05	-8.39	2.60E+05	-1.89	8.13E+04	-3.21
3	120	5.01E+05	-4.39	2.58E+05	-0.77	7.99E+04	-1.72

Sector Angle	No. of sectors	Vertical Deflection (mm)	Number of cycles	Distance (Miles)	Maximum Tire Temperature (C)
6	60	23.6	4.24E+07	48337	51.1
4	90	23.6	4.16E+07	47425	51.0
3	120	23.6	4.16E+07	47425	51.9

6.1.2 Thermal profile and predicted fatigue life

Before carrying out thermal and fatigue life simulations, freerolling simulation was used to get the freerolling angular speed and freerolling radius for both tire sizes. The rolling radii are listed in Table 6.2 with the rolling radius of the 18-inch tire being 36 mm more than the rolling radius of the 14-inch tire. The period of one rotation of tire at 45 mph was used for thermal and fatigue life simulations. Temperature profile and predicted fatigue life of the tires is shown in Figure 6.2. The red areas in fatigue life plots indicate regions with minimum fatigue life and these would be the critical areas. The critical elements with the lowest predicted fatigue life are marked with a yellow circle which for the 14-inch base tire lies in the sidewall component at the ply edge and for the 18-inch base tire lies in the sidewall component adjacent to the rim contact area. The belt edges also show low predicted life cycles (of the order of 1E8) but the values are more than those at the critical elements. Most modern tires have belt edge cushions or gum strips wrapping around belt edges to

reduce stress concentration and improve fatigue life. These are also present in the tire models used in this work which might be the reason why belt edges do not turn out to be the critical regions in the simulation results. Although the 18-inch tire is only a scaled version of the 14-inch tire, the difference in critical region between the two is due to the change in aspect ratio of the tires and higher stresses in the rim contact region. Comparing the temperature profile, the 18-inch tire shows a maximum temperature of 46.1°C while the 14-inch tire shows a maximum temperature of 51.7 °C.

From Table 6.2 we can see that both tire sizes have comparable rolling resistance values. The 18-inch tire has higher predicted life cycles than 14-inch tire and combined with a larger rolling radius gives a distance travelled before failure of 70980 miles as compared to 47650 miles for the 14-inch tire.

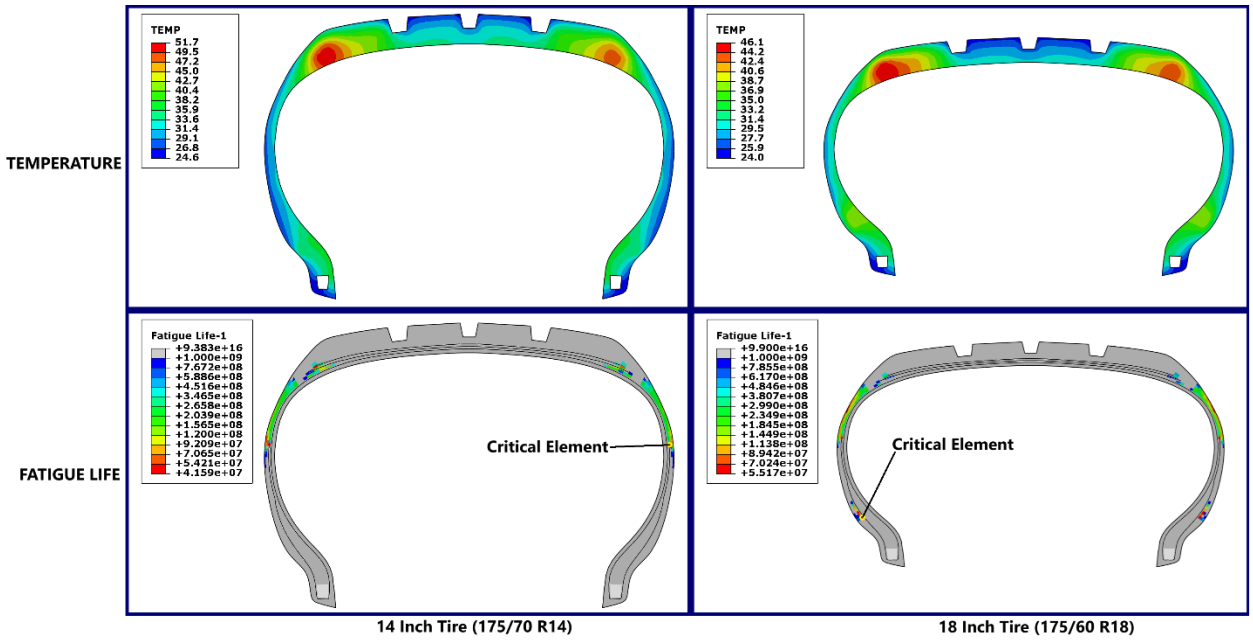

Figure 6.2 Temperature profile and predicted fatigue life for 14- and 18-inch base tires

Table 6.2 Predicted life cycles, distance before failure and rolling resistance for base 14-inch and 18-inch inflated tires rolling at 45 mph

Tire Size	Rolling Radius (mm)	Angular Velocity (rad/s)	Predicted Life Cycles	Distance (Miles)	Rolling Resistance (kg/T)
175/70 R14	293.4	68.54	4.16E+07	47650	7.5
175/60 R18	329.4	60.90	5.52E+07	70980	7.2

6.2 Results for insert supported run-flat system

The design for insert supported run-flat system was completed in two phases. The results of the preliminary design study with a rigid insert are discussed first followed by the design and results of a deformable rubber insert. The insert supported system design study was only conducted for the 14-inch tire.

6.2.1 Clearance study with preliminary designs

It is essential that a clearance between the insert and tire inner surface is maintained in inflated running conditions. For this, the clearance between insert surface and tire inner surface has been studied for 100% and 140% of rated loads. Having clearance between the insert and tire surface is essential because the tire deformation increases for load cases like overloading, pothole and curb impact and it must be ensured that the contact does not occur during the normal inflated running condition. Since simulating pothole and curb impact loading is computationally expensive and would require additional parameters like suspension stiffness to get accurate results, a maximum loading condition of 140% of rated load was instead used to consider such scenarios. Figure 6.3 shows the deflection of tire structure and the resulting clearance between the insert and tire surface for 100% and 140% loads. The clearance is also listed in Table 6.3. It is seen from the clearance values in the table that all insert heights have clearance greater than 5 mm when loaded with 100% rated load, but the value of clearance becomes zero for 80 mm insert height with 140% load. This implies that an 80 mm height insert would be in continuous contact with the tire surface if tire is running in overloaded condition or it would abruptly come in contact and

cause transfer of a high amount of impact forces to the rim in case of pothole and curb impacts. The insert height of 80 mm is thus not acceptable. Although the design with 80 mm insert height is rejected based on this study, the other results for this height are still included for completeness.

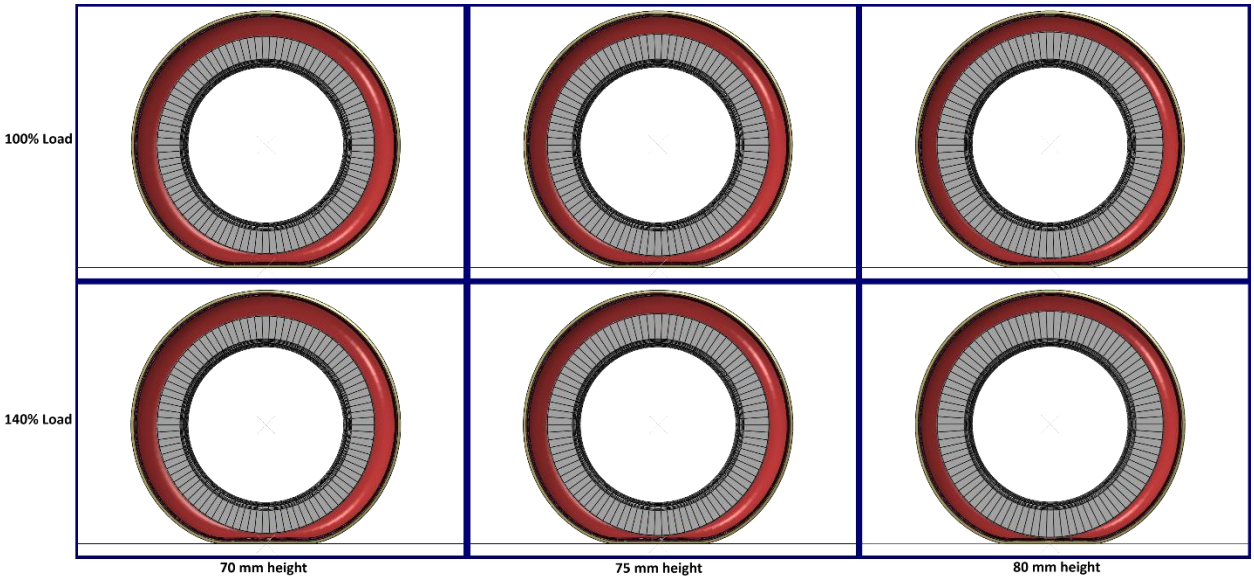

Figure 6.3 Deflection of tire and clearance between insert and tire surface for different loads

Table 6.3 Clearance between insert and tire inner surface for different insert heights with 100% and 140% loads

Insert Height (mm)	Clearance (mm) @ 100% load	Clearance (mm) @ 140% load
70	16.9	8.8
75	11.9	3.8
80	6.9	0

6.2.2 Results of preliminary design study

In this section the structural, thermal and fatigue results for the preliminary study for the insert supported design are discussed.

6.2.2.1 Strain Energy Density of deformed tire structure

Strain energy density can be used as a parameter to predict tire heat generation as well as tire fatigue life. The highest strain energy density in deflated condition for the preliminary study designs was found in the sidewall region. Figure 6.4 shows the SED distribution for all designs for the sidewall component. The designs with lower heights lead to larger deformation of the sidewall which results in higher SED. This trend is observed for both 60 mm and 80 mm insert widths. The difference between 60mm and 80 mm designs is less than 10% for the same height with the 80 mm designs having higher SED values.

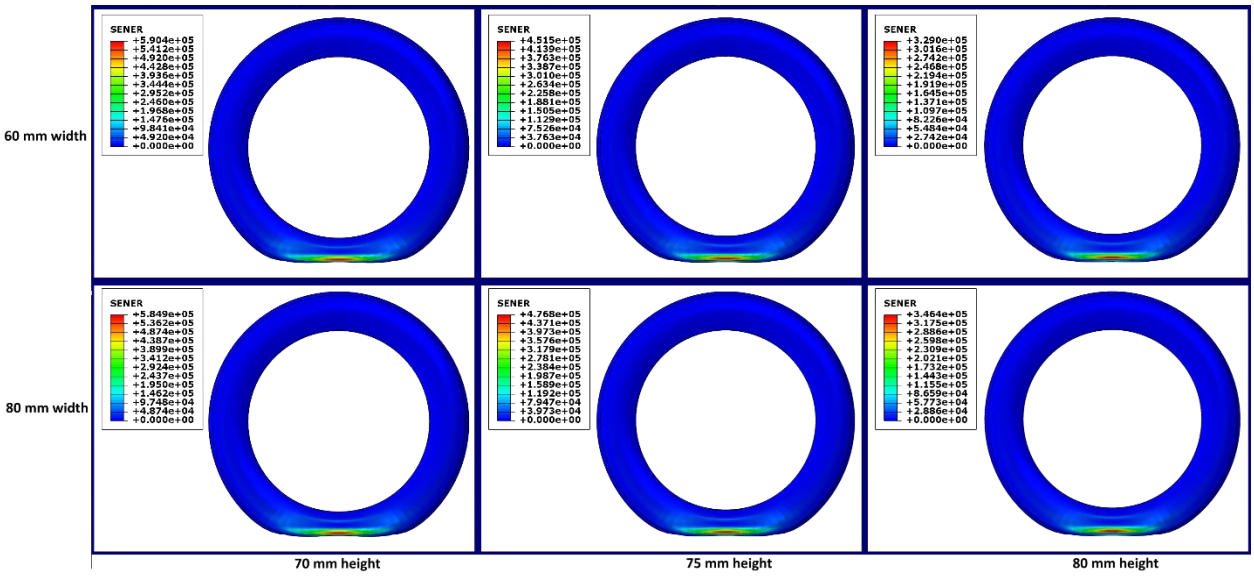

Figure 6.4 Strain Energy Density in sidewall component in deflated condition for different rigid insert width and height

6.2.2.2 Contact area and contact pressure

Figure 6.5 shows the contact pressure distribution for the preliminary designs. In deflated condition, the majority of load is supported by the insert while a fraction of the total load is also supported by the tire structure. It was thus expected to have higher contact pressure

in the region where tire inner surface is in contact with the insert. Larger contact area available in the wider designs would lead to higher contact patch area also lower maximum contact pressure. This is also observed in the results with 80 mm designs having higher contact area and 20% less maximum contact pressure. With increasing insert height, contact area shows a slight decrease together with a small increase in the maximum contact pressure.

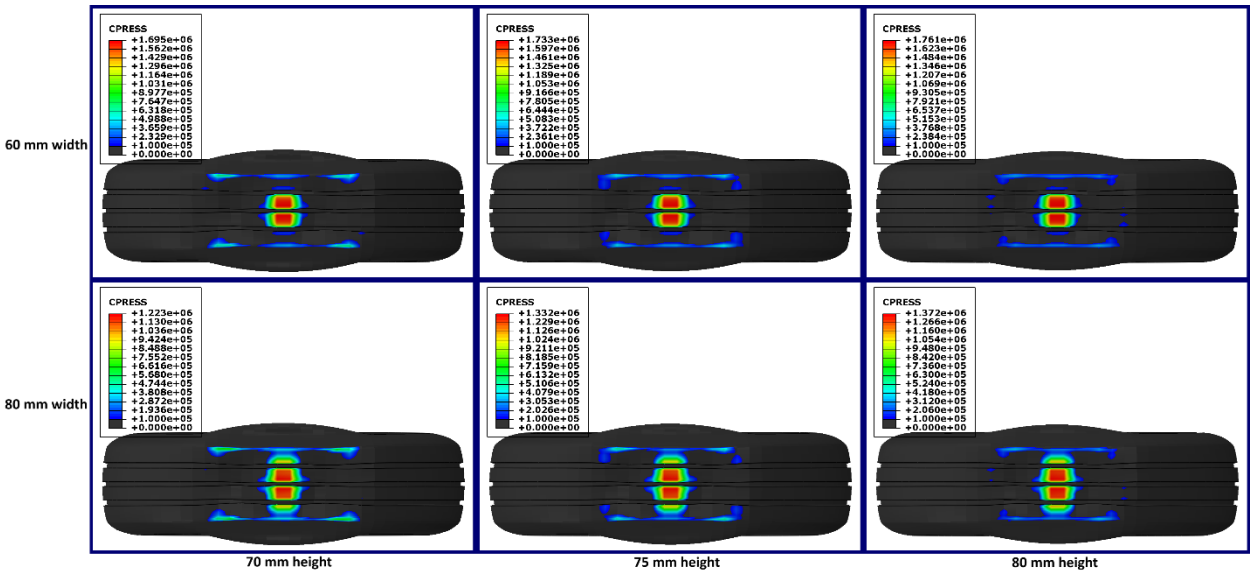

Figure 6.5 Contact patch shape and contact pressure for the preliminary ISR designs in deflated condition

6.2.2.3 Tire fatigue life and temperature profile

Tire fatigue life is the major performance criteria for the design process. Fatigue life and temperature have a strong dependence on the variation of SED in a revolution of tire. Fatigue life also has a strong dependence on the temperature profile. For the preliminary designs, instead of finding the accurate value of rolling radius, an approximate value of 292 mm was used for computing the freerolling angular speed and the time period of one revolution. The temperature profile and fatigue life simulations were carried using this time period.

Figure 6.6 shows the temperature profile for the preliminary designs. The maximum temperature is observed in the tread/crown region, and it is higher for designs with 60 mm width because of higher stresses due to higher contact pressures in the region. Designs with lower heights have higher heat generation in the sidewall and inner liner due to additional flexing which leads to higher temperatures.

Figure 6.7 shows the predicted life cycles for the preliminary designs. The red region marks the lowest life and thus the critical regions where failure would occur first. The upper sidewall region is the critical region for fatigue life. Table 6.4 lists the predicted fatigue life and the distance travelled before failure for the designs. Due to lower deformation, the designs with higher height have higher predicted life while the values for 60 mm and 80 mm width do not show a clear trend and have similar values. Although the maximum temperature is higher for the lower width design, the temperatures in the critical region are similar and thus the effect of higher temperature is not observed in the predicted fatigue life.

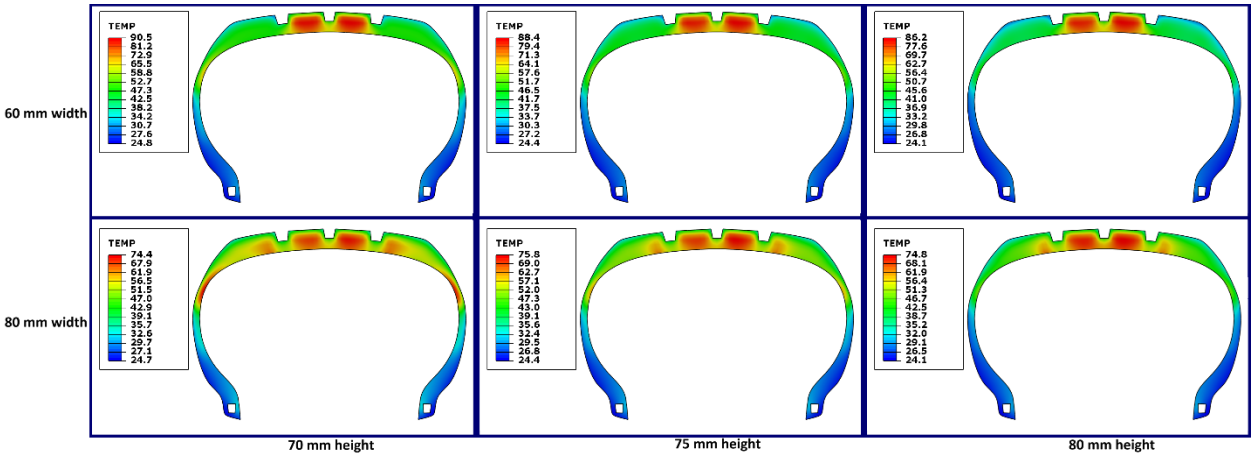

Figure 6.6 Temperature profile of tire section for the preliminary ISR designs in deflated condition at 45 mph speed

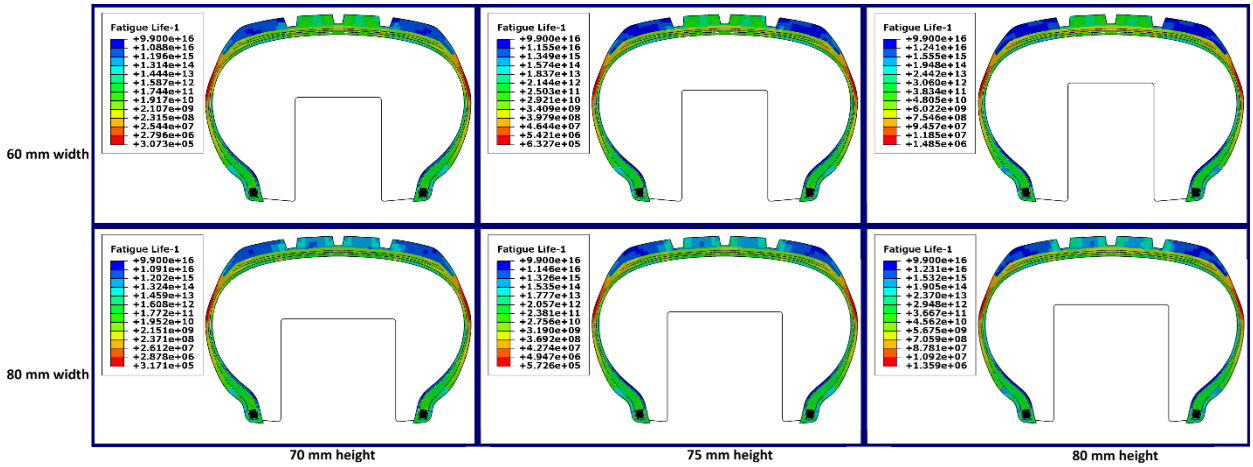

Figure 6.7 Predicted fatigue life cycles for the preliminary ISR designs in deflated condition at 45 mph speed

Table 6.4 Predicted life cycles and distance before failure for the preliminary ISR designs in deflated condition at 45 mph speed

Design Dimensions (Width X Height) (mm X mm)	Predicted Life Cycles	Distance before failure (Miles)
60X70	3.07E+05	350
60X75	6.32E+05	720
60X80	1.48E+06	1687
80X70	3.17E+05	361
80X75	5.72E+05	652
80X80	1.36E+06	1550

6.2.3 Results for insert supported design with a deformable insert

Based on the results in the previous section, it was decided to keep the dimensions of the insert to be 80 mm width and 75 mm height. 75 mm height is chosen to have a higher fatigue life with an acceptable clearance between tire and insert. A width of 80 mm is selected because of the higher contact area and lower contact pressure along with a lower maximum temperature of the tire.

For the deformable design, cylindrical rubber inserts of thickness 5 mm and 10 mm and reinforced by ply fiber of cross section area and spacing same as the body ply of tire was used. The design can be described as a 'tire within a tire' and is shown in Figure 6.8 . The 5 mm design was not able to support the rated load in structural simulation study and was rejected as a potential design. The results for the 10 mm thick design are discussed in this section.

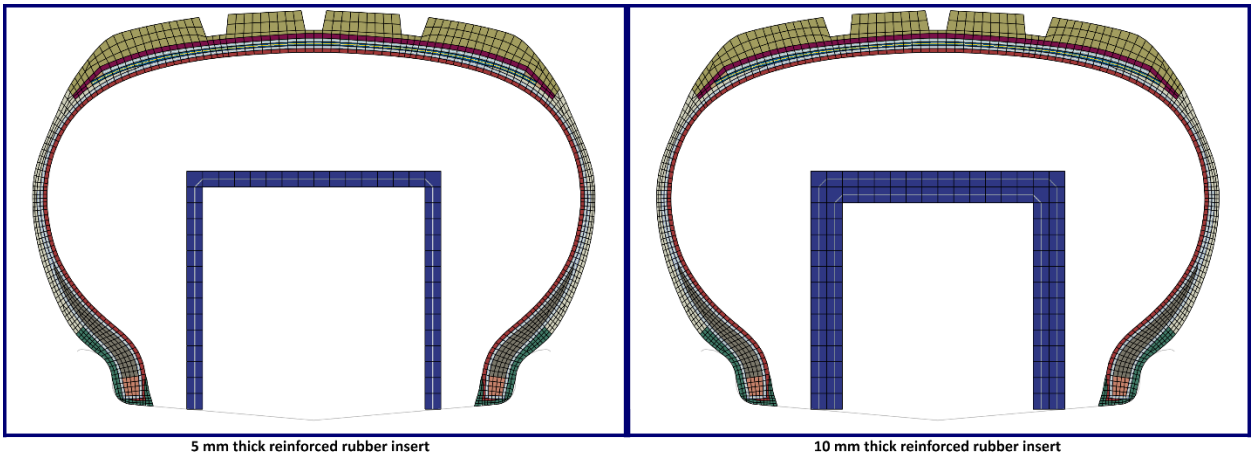

Figure 6.8 Potential deformable insert designs

6.2.3.1 Strain energy density, contact area and contact pressure

Figure 6.9 shows the SED and contact pressure distribution for the design. The maximum SED at sidewall is higher than that observed for the rigid design of similar dimensions. Also, compared to the rigid insert design, the contact area in the deformable design decreased with the contact shifting to the shoulder of the tire. The reduction of contact area also

caused an increase in maximum contact pressure. The bending of the flat face of the insert leads to loss of contact around the center groove of the tire. This design topology can be used to further optimize the shape of the design to get a better contact area and contact pressure distribution.

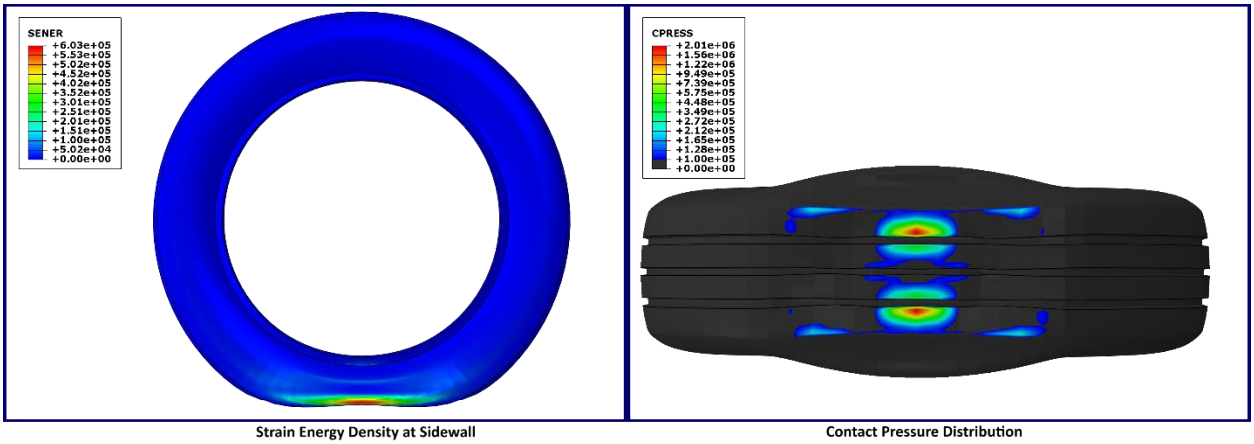

Figure 6.9 SED and contact pressure for the deformable ISR tire design

6.2.3.2 Fatigue life and temperature profile

The temperature profile and predicted fatigue life of the tire structure and deformable design are shown in Figure 6.10. The results show similar temperature profile and maximum temperature value as the rigid design with an additional higher temperature area at the inner liner. Maximum temperature of tire structure is predicted to be 78°C with the temperature of insert structure remaining below 60°C. It was expected that the deformable design would have lower fatigue life compared to the rigid 80X75 mm design which turned out to be correct with the predicted life is 2.95E5 cycles equivalent to a distance before failure of 340 miles. The critical region in the sidewall where the tire is expected to fail first is marked in the figure with a yellow circle.

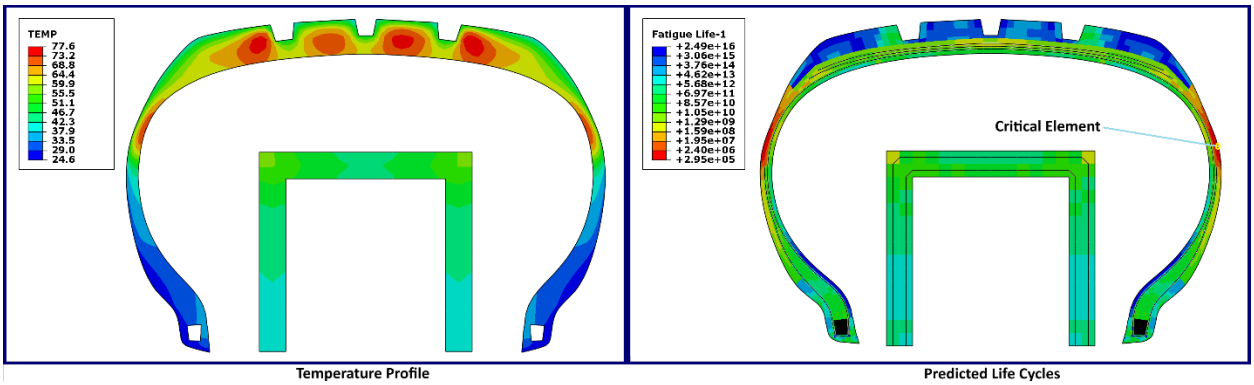

Figure 6.10 Temperature profile and predicted fatigue life for the deformable ISR tire design

6.3 Results for self-supporting run-flat system

In this section, the results for the 6-candidate designs for the self-supporting run-flat system are first discussed. Based on the results, one design is selected for further studies for parameters related to ride and handling performance. In the last part, the selected design is scaled to the 18-inch tire dimensions and the same performance parameters are studied for this scaled design.

6.3.1 Results for candidate designs

In this section the structural, thermal and fatigue simulation results for the candidate designs for the self-supported run-flat tire are discussed. Due to convergence issues, the structural simulations for the 10 mm thickness designs were carried by using a sector angle of 2.5° instead of 4°.

6.3.1.1 Strain Energy Density

Figure 6.11 shows the SED in deflated conditions. The maximum values are observed in the inner liner component followed by sidewall. Maximum SED for 10 mm thick designs is 50% higher than the corresponding 15 mm thick designs. The 10 mm designs also have a higher vertical deflection with the crown region bending enough that the neighboring tread blocks come in contact and close the center groove. It can be inferred from the deformation that the thinner designs are barely supporting the load.

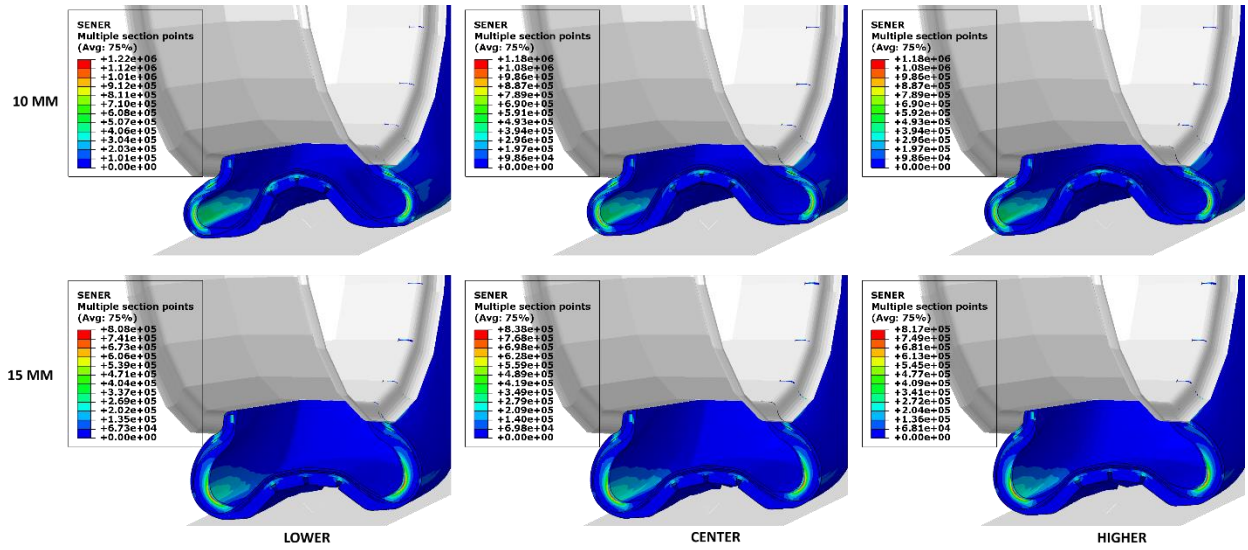

Figure 6.11 SED for SSR designs in deflated condition

6.3.1.2 Contact Patch

Figure 6.12 shows the contact pressure distribution at the road-tire contact surface for the designs in deflated condition. In the insert supported design, the tire tread/crown area was in contact with the road and insert and supported majority of the load while in these designs, this area bends up and loses contact with the road and only the shoulder region remains in contact. This was already observed in the deflected shape in Figure 6.11 and can also be inferred from the contact patch shape which shows pressure distribution only in the shoulder region. While the 15 mm designs have continuous contact at the shoulder, the 10 mm designs do not. The maximum contact pressure value does not vary a lot with design and is around 1.5 MPa for all designs.

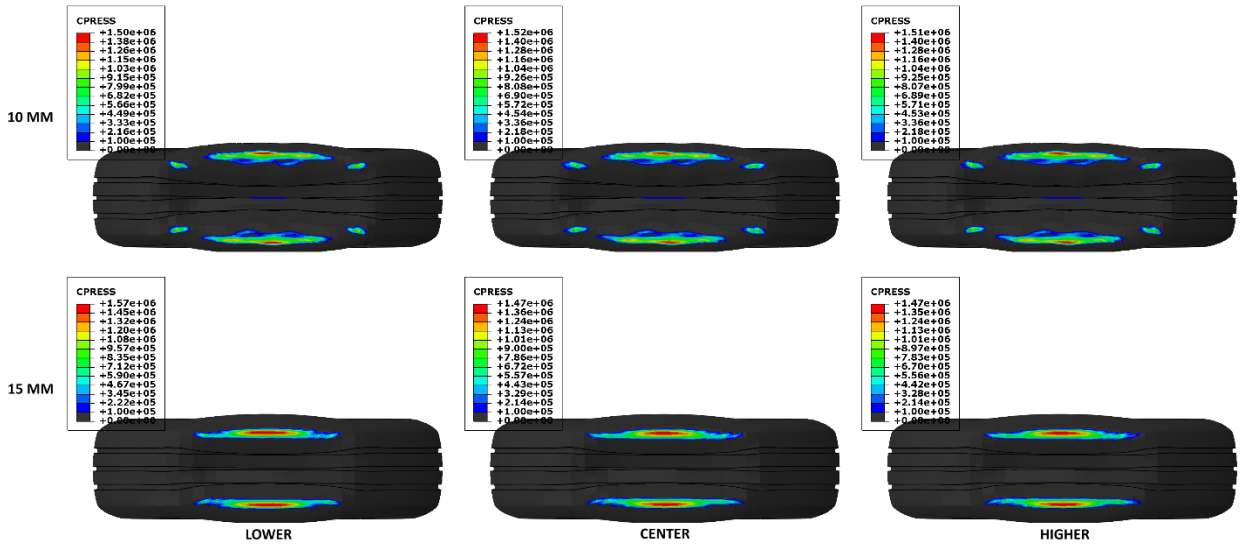

Figure 6.12 Contact patch for SSR designs in deflated condition

6.3.1.3 Fatigue Life and Temperature Profile

The fatigue and thermal simulation were carried by assuming an approximate value for the rolling radius for each design. Figure 6.13 shows the temperature profile for all potential designs. The 10 mm thick designs show higher values of temperature across the cross section with maximum values reaching 160 °C. This is a very high temperature, and rubber starts degrading rapidly at such temperatures. The maximum temperatures values are observed in the region around belt edges and some parts of the inner liner and insert. The 15 mm designs show maximum temperatures around 130 °C with the maximum values occurring at the inner liner and added supporting insert component. The higher temperature in belt edge region for 10 mm thick designs can be explained by the additional bending occurring in this region.

Figure 6.14 shows the fatigue life cycles for the designs which are summarized in Table 6.5 including the predicted distance before failure and the computed rolling resistance values. All 10 mm designs show similar values of rolling resistance and so do the 15 mm designs irrespective of the starting position of the reinforcing rubber. The 10 mm designs would be good enough only for a distance of 2 miles before they fail while all the 15 mm designs have

a distance before failure greater than 50 miles with the ‘lower’ design having the highest value of 96 miles. As was clear from the SED and deformations seen in Figure 6.11, the fatigue life results clearly indicate that the designs with 10 mm sidewall thickness are structurally not stiff enough to support the load and result in very low tire fatigue life cycles. Among the 15 mm designs, the one with ‘lower’ design gives the best tire fatigue life. This design would be considered as the final design for further studies in the next section.

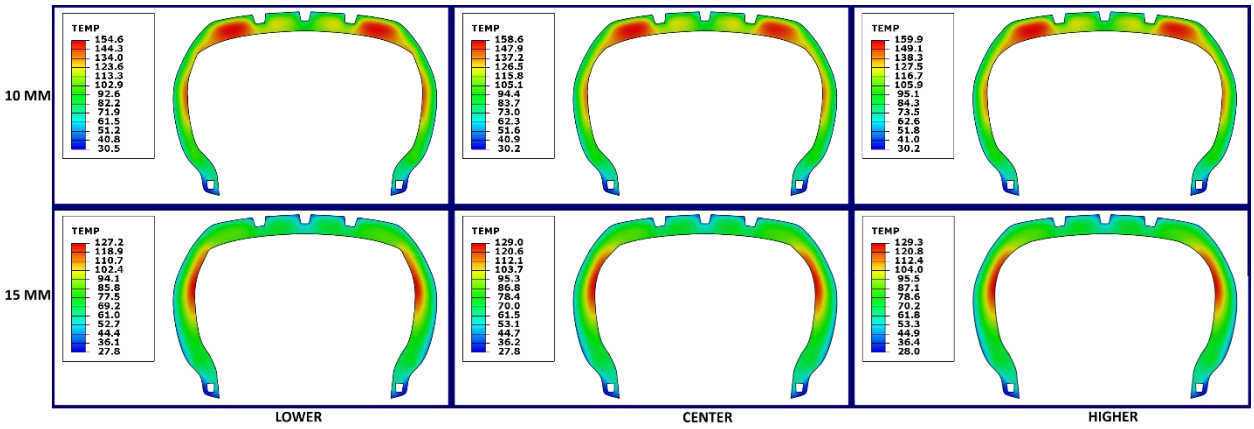

Figure 6.13 Temperature profile for SSR designs in deflated condition at 45 mph speed

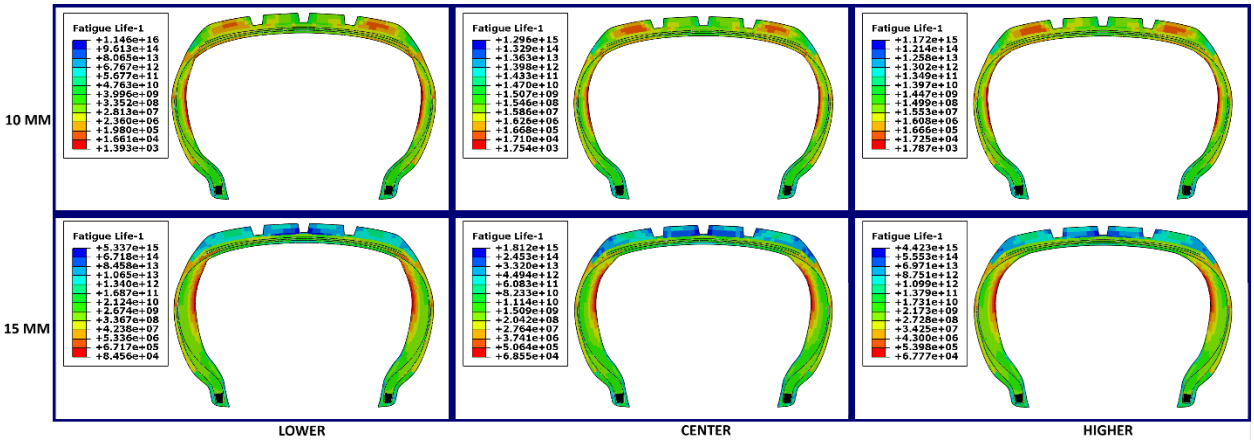

Figure 6.14 Fatigue life for SSR designs in deflated condition at 45 mph speed

Table 6.5 Predicted life cycles, distance before failure and rolling resistance for SSR designs in deflated condition at 45 mph speed

Design	Approximate Rolling Radius (mm)	Angular Velocity (rad/s)	Predicted Life Cycles	Distance (Miles)	Rolling Resistance (kg/T)
10 mm lower	291	69.11	1.39E+03	2	74.5
10 mm center	292.1	68.85	1.75E+03	2	74.8
10 mm higher	292.1	68.85	1.79E+03	2	75.2
15 mm lower	292	68.87	8.46E+04	96	39.9
15 mm center	292.2	68.82	6.85E+04	78	40.0
15 mm higher	291.6	68.96	6.78E+04	77	40.2

6.3.2 Results for 14-inch self-supporting run-flat tire design

6.3.2.1 Fatigue life and temperature profile

Since the fatigue life listed in the previous section was computed using an approximate value for the rolling radius, in this section rolling simulation is performed for the selected design to accurately estimate the rolling radius and fatigue life. From freerolling simulation in deflated condition at 45 mph, the freerolling angular velocity was found to be 69.06 rad/s which corresponds to a rolling radius of 291.17 mm. These values are close to the ones used in the previous section. As a result, the predicted fatigue life cycles 8.30E4 and the distance before failure of 94 miles were also similar to those in the previous section. The predicted rolling resistance was 40.0 which is more than 5 times the value of 7.5 for the base tire. The rolling resistance values from Table 6.6 also show that the run-flat design has a higher rolling resistance value (8.9) than the base tire. This is due to the addition of reinforcing rubber material in the run-flat design which causes additional energy loss.

From these results, we can also conclude that an approximate rolling radius can be used for fatigue life calculations without going for the freerolling simulations and the freerolling simulations are only necessary if it is also required to do cornering simulations to predict lateral force generation.

Figure 6.15 shows the temperature profile of the final design and predicted fatigue life. The critical element with the lowest fatigue life is in the inner liner component and the temperature at the element is 126.4 °C.

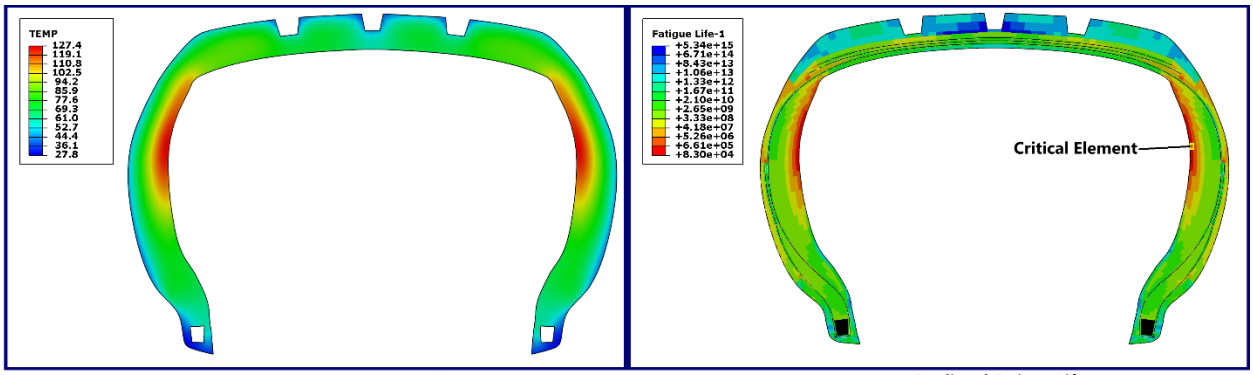

Figure 6.15 Temperature profile and predicted fatigue life for 14-inch SSR tire design in deflated condition at 45 mph

Table 6.6 Fatigue life, distance before failure and rolling resistance for 14-inch base and SSR tire at 45 mph

Tire	Rolling Radius (mm)	Angular Velocity (rad/s)	Predicted Life Cycles	Distance (Miles)	Rolling Resistance (kg/T)
Inflated base tire	293.41	68.54	4.16E+07	47650	7.5
Inflated run-flat tire	294.22	68.35	3.83E+07	43990	8.9
Deflated run-flat tire	291.17	69.06	8.30E+04	94	40.0

6.3.2.2 Lateral force generation and handling

Figure 6.16 shows the shape of contact patch at 45 mph with 4 degree slip angle for inflated base tire, inflated SSR tire and deflated SSR tire. In inflated condition, the contact patch shifts towards the direction of slip and the size of the patch becomes smaller in the opposite side. Similar trend is observed in the first two shapes. For the deflated condition, although the contact length decreases for the side opposite to the direction of slip, the contact pressure at the shoulder has high contact pressure values. Additionally, some contact is established at the edges of the patch which was not in contact in static and no slip rolling condition (Figure 6.12).

The lateral force variation with slip angle is plotted in Figure 6.17. In inflated condition, both base and SSR tire produce similar lateral forces with the SSR tire producing slightly more lateral force for smaller slip angles. The lateral force for different slip angles is summarized in Table 6.7 and it is observed that the lateral forces in the deflated SSR tire are almost half of those generated in an inflated SSR tire. This is a significant decrease and would be easily perceivable by the driver when cornering.

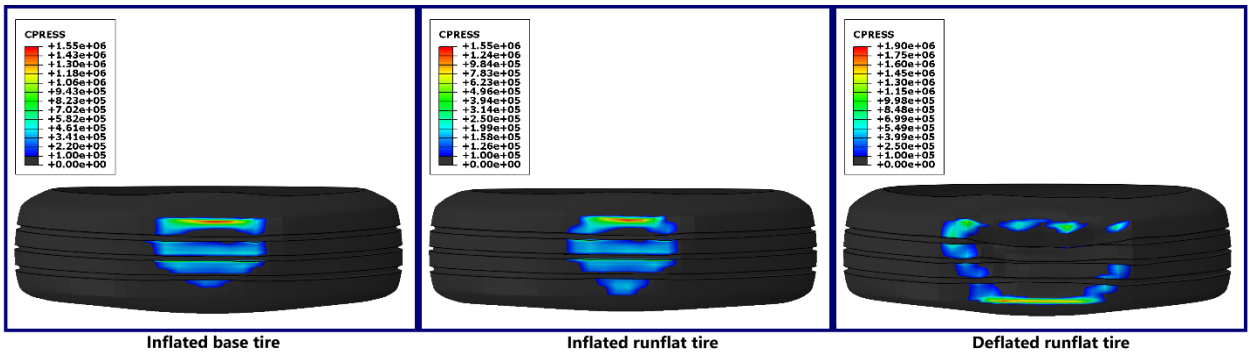

Figure 6.16 Contact patch at 4 degree slip angle for 14-inch inflated base, inflated SSR and deflated SSR tire

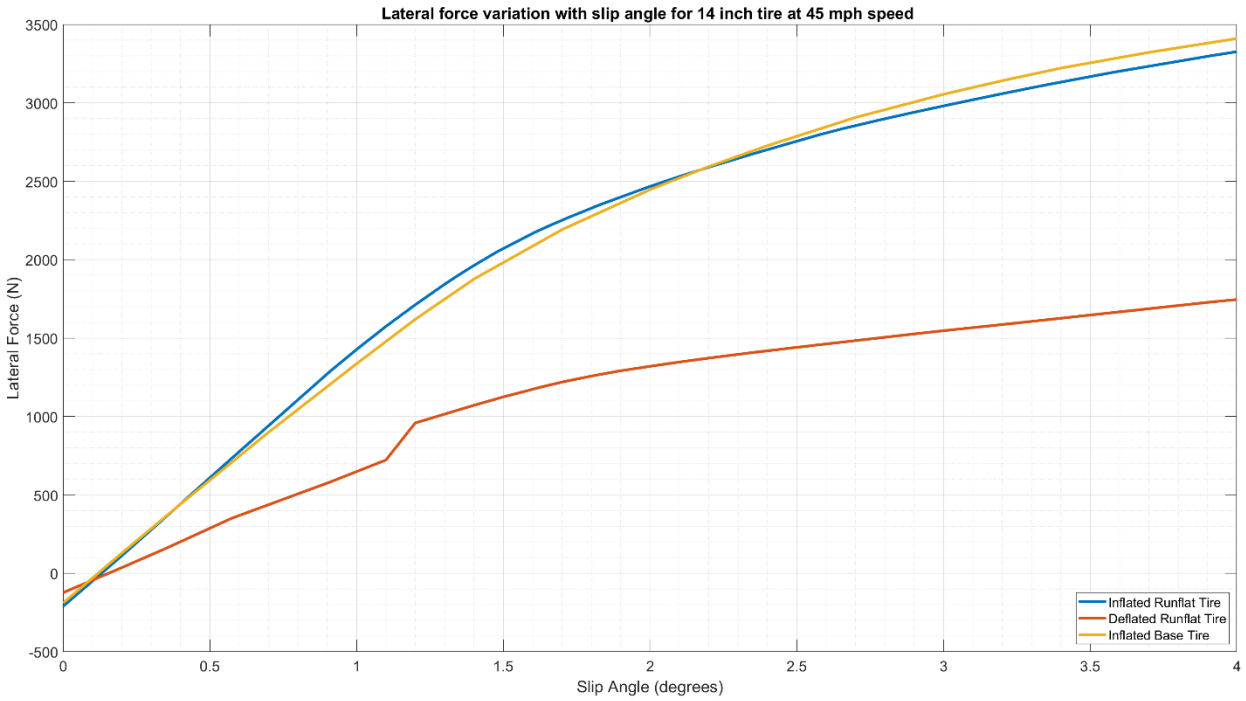

Figure 6.17 Lateral force variation with slip angle for 14-inch inflated base, inflated SSR and deflated SSR tire at 45 mph

Table 6.7 Lateral force at different slip angles for 14-inch tire at 45 mph

	Lateral Force (N)		
Slip Angle	**Inflated base tire**	**Inflated SSR tire**	**Deflated SSR tire**
0	-190	-210	-123
1	1336	1427	648
2	2446	2467	1320
3	3055	2980	1547
4	3410	3326	1746

6.3.2.3 Vertical stiffness and ride quality

Figure 6.18 shows the load deflection curve for the 14-inch inflated base tire, inflated SSR tire and deflated SSR tire. The dotted lines mark 100% and 140% rated loading force. The inflated SSR tire has the highest stiffness value and the deflection at 100% load is 18.5 mm compared to the inflated base tire which has a deflection of 24 mm. The deflated SSR tire is least stiff with a deflection of 39.5 mm at 100% load. This can be verified with the average stiffness values listed in Table 6.8. The stiffness of the inflated SSR tire can be interpreted to be the sum of stiffness of inflated base tire and deflated SSR tire. This curve can also be used to estimate the contribution of structure in the total stiffness of an inflated SSR tire. At 100% load i.e. 18.5 mm deflection, it is observed that close to 30% of the stiffness is due to the structure. This contribution % would be lower for a non-run-flat tire.

While average stiffness can be used to gauge tire deflection with load, the operating point stiffness gives a better view of the force generated for small deflections in the loaded condition. From the stiffness values listed in Table 6.8, the operating stiffness values are higher than the average stiffness values which shows that the tire structure is becoming stiffer with increasing deflection. The operating point stiffness values at 100% load are similar for the inflated base tire and deflated SSR tire although the deflated SSR tire achieves this stiffness at a higher deflection value. The operating point stiffness for inflated SSR tire is 50% higher than that of the inflated base tire. This significant increase in operating point stiffness would lead to inferior ride quality for the SSR tire in normal inflated running condition due to higher dynamic load transfer to the wheel and suspension. The difference would be much more perceptible when the tire goes over potholes and rough roads.

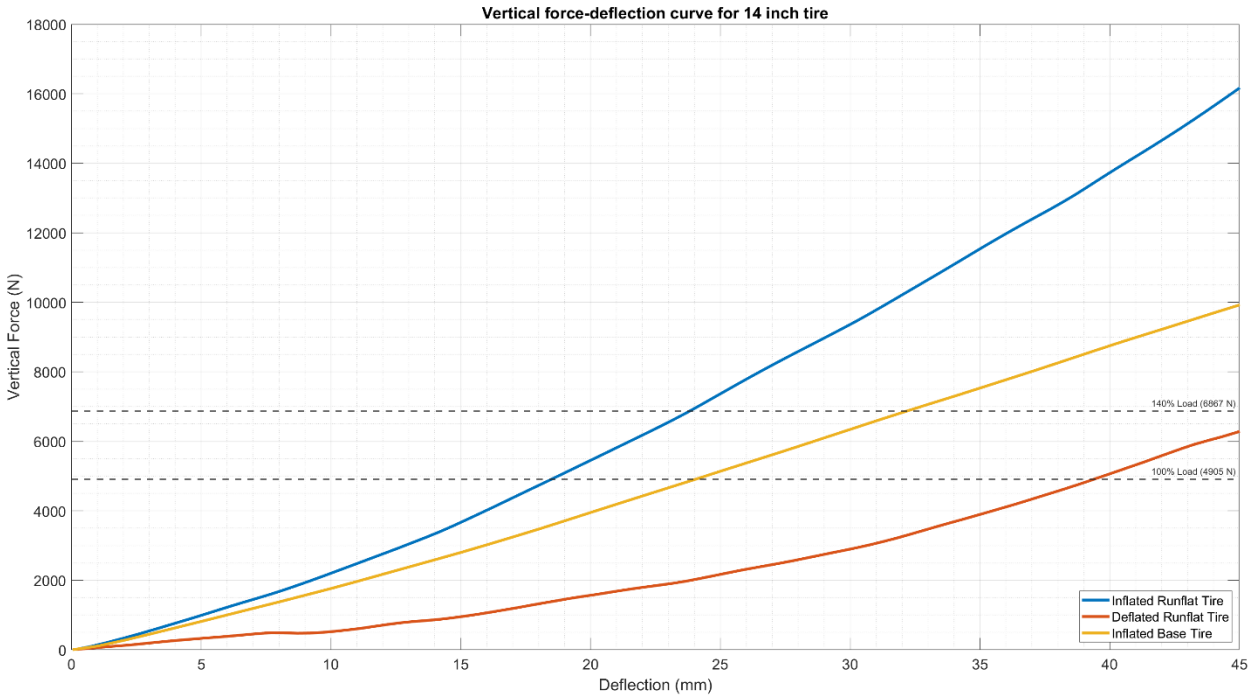

Figure 6.18 Force-Deflection curve for 14-inch inflated base tire, inflated SSR tire and deflated SSR tire

Table 6.8 Average and operating point stiffness at 100% load for 14-inch inflated base tire, inflated SSR tire and deflated SSR tire

	Stiffness (N/mm) at 100 % load (4905 N)	
Tire	**Average stiffness**	**Operating point stiffness**
Inflated base tire	204	241
Inflated SSR tire	266	361
Deflated SSR tire	124	256

6.3.2.4 Bead unseating risk assessment

Introduction of slip angles leads to uneven distribution of contact pressure between the left and right sides of the tire. Very large slip angles can lead to the tire bead area losing contact with the rim causing 'bead unseating'. In this part of the results, the contact pressure distribution in the tire-rim contact area will be discussed for different slip angles.

Figure 6.19 shows the contact pressure distribution at rim contact surface for deflated SSR tire with slip angles of 0,1 and 4 degrees. '+Y' being the direction of slip, the surface in the direction of slip shows high contact pressure in the bead seat area and is held in place by friction between tire and rim. For the opposite side, the tire is losing contact with the bead-seat and the contact pressure at the rim flange provides lateral force and holds the tire in place by friction. Although partial bead unseating is observed, overall, the run-flat design can be considered safe from bead unseating issues for a slip angle of 4 degrees.

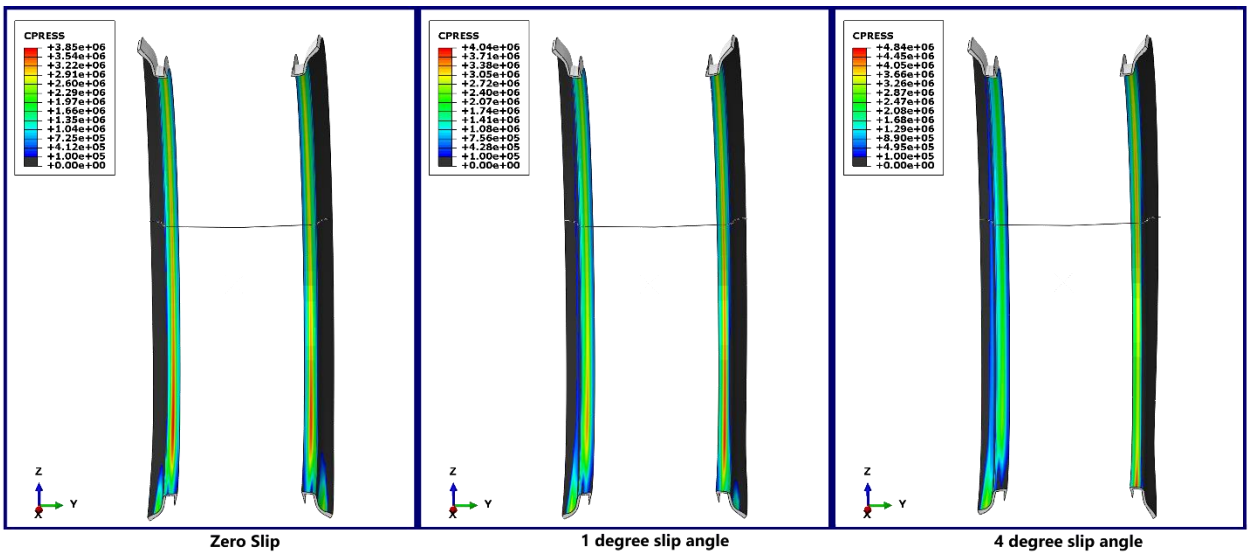

Figure 6.19 Contact pressure distribution on the rim contact surface for 14-inch SSR tire in deflated condition at varying slip angles

6.3.3 Results for 18-inch self-supporting run-flat tire design

The 18-inch SSR tire design was constructed by scaling the 14-inch SSR tire using ETRTO standard as listed in Table 4.2. The results for this scaled tire are discussed in this section.

6.3.3.1 Fatigue life and temperature profile

The fatigue life and temperature profile simulations were carried using the freerolling angular velocity of 61.15 rad/s found using freerolling simulation. The freerolling radius was found to be 328.8 mm. With the predicted fatigue life cycle value of 1.06E5, the distance before failure was computed to be 136 miles. This predicted value is higher than that of the 14-inch SSR tire because of higher fatigue life and a higher rolling radius. From the data in Table 6.9, the predicted rolling resistance was 33 which is lower than that of the 14-inch version. Also, the rolling resistance for the run-flat tire increased to 8.9 from 7.2 for the base tire. Figure 6.20 shows the temperature profile and predicted fatigue life. The critical element with the lowest fatigue life lies in the inner liner component and the temperature at the element is 119.2 °C which is slightly lower than the temperature at the critical element of 14-inch SSR tire.

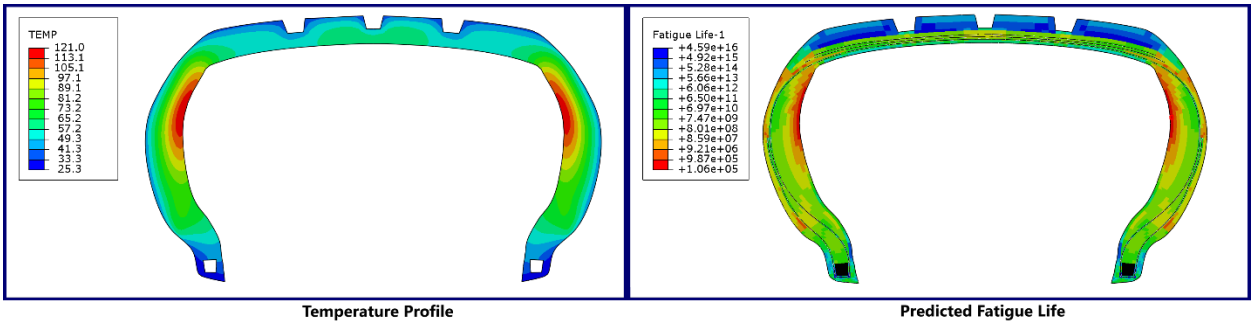

Figure 6.20 Temperature profile and predicted fatigue life for 18-inch SSR tire at 45 mph

Table 6.9 Fatigue life, distance before failure and rolling resistance for 18-inch base and SSR tire at 45 mph

Tire	Rolling Radius (mm)	Angular Velocity (rad/s)	Predicted Life Cycles	Distance (Miles)	Rolling Resistance (kg/T)
Inflated base tire	329.40	60.9	5.52E+07	70990	7.2
Inflated run-flat tire	330.98	60.76	4.76E+07	61510	8.9
Deflated run-flat tire	328.84	61.15	1.06E+05	136	33.0

6.3.3.2 Lateral force generation and handling

The lateral force variation with slip angle at a speed of 45 mph for 18-inch inflated base, inflated SSR and deflated SSR tire is plotted in Figure 6.21. In inflated condition, both base and SSR tire produce similar lateral forces with the SSR tire producing slightly more lateral force for smaller slip angles. From the data in Table 6.10 it can be observed that for same slip angles, the 18-inch base and SSR tire in inflated condition generate more lateral force than the 14-inch base and SSR tire respectively (Table 6.7). Similar trend was expected for the lateral force generated by the 18-inch SSR tire in deflated condition, but it was found that in deflated condition, the 18-inch SSR tire generated less lateral force than the 14-inch SSR tire.

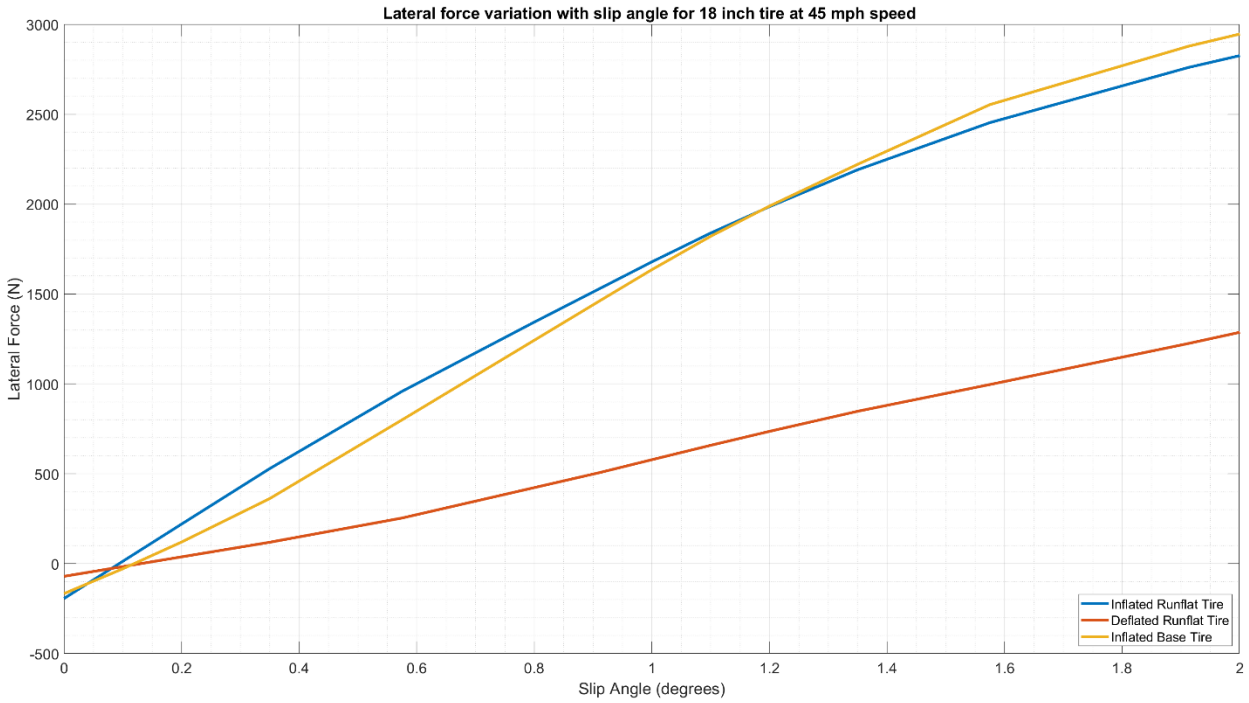

Figure 6.21 Lateral force variation with slip angle for 18-inch inflated base, inflated SSR and deflated SSR tire at 45 mph

Table 6.10 Lateral force at different slip angles for 18-inch tire at 45 mph

	Lateral Force (N)		
Slip Angle	**Inflated base tire**	**Inflated SSR tire**	**Deflated SSR tire**
0	-166	-194	-70
1	1635	1679	578
2	2946	2826	1287

6.3.3.3 Vertical stiffness and ride quality

Figure 6.22 shows the load deflection curve for the 18-inch inflated base, inflated SSR and deflated SSR tire. The dotted line marks 100% rated loading force of 5052 N. The inflated SSR tire has the highest stiffness value and the deflection at 100% load is 17 mm compared to the inflated base tire which has a deflection of 24 mm. The deflated SSR tire is least stiff with a deflection of 31 mm at 100% load. This can also be observed from the

average stiffness values listed in Table 6.11. The tire-structural stiffness of the 14- and 18-inch SSR tires can be compared by comparing the average stiffness in deflated condition. In deflated condition, the average stiffness of 18-inch SSR tire (164 N/mm) is 30% higher than the average stiffness of 14-inch SSR tire (124 N/mm).

The operating point stiffness of the 18-inch SSR tire in inflated condition (425 N/mm) is 18% higher than that for the 14-inch SSR tire in inflated condition (361 N/mm). The ride quality would thus further deteriorate when using the 18-inch run-flat tire.

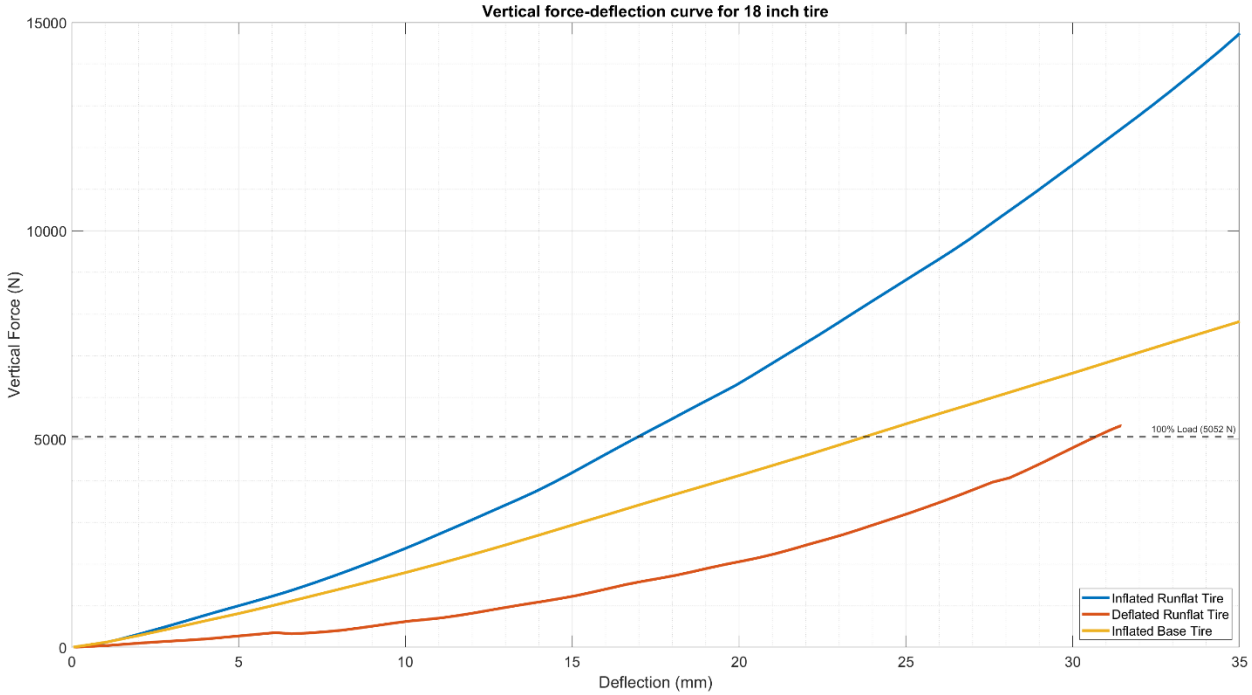

Figure 6.22 Force-Deflection curve for 18-inch inflated base tire, inflated SSR tire and deflated SSR tire

Table 6.11 Average and operating point stiffness at 100% load for 18-inch inflated base tire, inflated SSR tire and deflated SSR tire

	Stiffness (N/mm) at 100 % load (5052 N)	
Tire	**Average stiffness**	**Operating point stiffness**
Inflated base tire	213	250
Inflated SSR tire	297	425
Deflated SSR tire	164	370

7 Conclusion and Future Work

The aim of this work was to establish a simulation-based framework for designing run-flat systems for tires. Both insert supported and self-supporting type of run-flat designs were explored, and different methodology was developed for each design type. A suitable design for each type was developed which satisfied the primary design target of achieving a distance travelled before failure of 50 miles at a maximum speed of 45 mph.

The work started with a mesh convergence study where a sector angle of 4° was decided to be used for structural simulations. The distance before failure for the base tire designs in inflated and loaded conditions at 45 mph was found to be 47650 and 70980 miles for the 14-inch and scaled 18-inch tire. These values are close to the expected life of commercially available tires and were used to verify the accuracy of the fatigue parameters.

From the results of the preliminary studies for the insert supported run-flat (ISR) systems, it was concluded that the lower insert height designs provide lower tire fatigue life due to higher deformations of the tire structure. For the deformable insert design, a hollow cylindrical structure made of reinforced 10 mm thick rubber of 80 mm width and 75 mm height was developed which showed an estimated distance before failure of 340 miles. The maximum temperature of tire structure was predicted to be 78° C with the temperature of insert structure remaining below 60° C. These temperatures are relatively low compared to the self-supporting designs. This design leaves a scope for further shape optimization to reduce material volume and improve other performance parameters like the contact patch size and shape.

The final design of self-supporting run-flat (SSR) system comprised of addition of an additional layer of rubber to reinforce the sidewall of the 14-inch base tire model to support the tire loads. This resulted in the thickness of the sidewall increasing to 15 mm with a total of 2.11 kg of rubber added to the tire. With this design a predicted distance before failure of 94 miles was achieved. The maximum temperature of the tire section reached 127° C which is considerably higher than the predicted operating temperature of inflated base tire

(52° C) and deflated tire with the insert supported design (78° C). Through the bead unseating study, it was found that the design would be safe for a slip angle of 4°. The robustness of the SSR design was verified with the scaled 18-inch tire model with a predicted distance before failure of 136 miles.

Although a run-flat tire offers safety and peace of mind, this work also helped in understanding the compromise that is made when using a SSR tire instead of a regular tire. The SSR tire has 20% higher rolling resistance leading to lower fuel economy and close to 50% increase in operating point stiffness due to stiffened sidewall would lead to a perceptibly inferior ride quality. The lateral force generation studies helped in understanding the limitations that a driver faces when the SSR tire is running in deflated condition. A close to 50% loss in the generated lateral force compared to the tire running in inflated condition would be significant enough to be subjectively felt by the driver who must be cautious and informed of the new handling characteristics. With tire scaling procedure, and the results of the 18-inch tire, it was understood that scaling can be used in certain situations to create different tire sizes successfully. It was also observed that changing the tire size or aspect ratio can change the areas of the tire structure which are critical in terms of tire life. It can be finally concluded that simulation can serve as a useful tool for the design of run-flat tire systems.

The following points can be considered to expand the scope and improve the accuracy of the results of the current work:

(1) Temperature and rolling resistance values were computed using a single set of hysteresis parameters for all rubber components. Components like the apex/bead filler rubber usually have higher heat generation properties compared to other components. Using different hysteresis properties for different rubber components would give better predictions, particularly for the self-supporting run-flat design where the operating temperature of the tire is higher.

(2) Although proving to be satisfactory for our design goals, the deformable insert supported design can be used as an initial geometry for further design optimizations to

save on material cost and improve other performance parameters. Further exploring the load supporting mechanism for the design can help in moving towards an optimal shape and dimensions for the insert.

(3) Automated optimization procedures can be used to get an optimal profile for the added rubber material in the SSR design. The optimization can be done to reduce the volume of added material while maintaining the tire fatigue life.

(4) While the effect on handling and ride qualities are briefly discussed, an expanded study including MBD simulations can be conducted to gain further insights of the handling performance of the run-flat tire. Including cleat impact simulations can further help in quantifying the impact on ride quality. Rolling simulations with different slip ratios to include braking and accelerating along with the results from different slip angles can be used to create a reduced tire model which is valid for a fully deflated tire for use in ride and handling MBD simulations.

(5) The accuracy of the simulation results specifically the fatigue life results need to be verified by building and testing physical tires.

8 References

[1] A. N. Gent and J. D. Walter, *Pneumatic tyre*, vol. Mechanical. 2006. [Online]. Available: https://ideaexchange.uakron.edu/mechanical_ideas/854/

[2] B. Rodgers, *Introduction to Tire Engineering*. 2020. doi: 10.1201/9781003022961-1.

[3] G. Leister, *Passenger Car Tires and Wheels*. 2018. doi: 10.1007/978-3-319-50118-5.

[4] "What's in a tire." U.S. Tire Manufacturers Association. [Online]. Available: https://www.ustires.org/whats-tire-0

[5] F. Philpott, R. Laske, and F. Montfort, "Run flat tires - Accomplishments of the Goodyear-Michelin joint venture," *SAE Tech. Pap.*, no. 724, 2004, doi: 10.4271/2004-01-1580.

[6] J. T. Alden, "The self-supporting tire: A new concept in vehicle mobility," *SAE Tech. Pap.*, 1977, doi: 10.4271/770349.

[7] A. Pannikottu, "Unclassified / Distribution A Approved for Public Release SURVIVABILITY ENHANCED RUN-FLAT VARIABLE FOOTPRINT TIRES Unclassified / Distribution A Approved for Public Release," 2010.

[8] H. Liu, Y. Pan, H. Bian, and C. Wang, "Optimize design of run-flat tires by simulation and experimental research," *Materials (Basel).*, vol. 14, no. 3, pp. 1–14, 2021, doi: 10.3390/ma14030474.

[9] J. R. Cho, J. H. Lee, K. M. Jeong, and K. W. Kim, "Optimum design of run-flat tire insert rubber by genetic algorithm," *Finite Elem. Anal. Des.*, vol. 52, pp. 60–70, 2012, doi: 10.1016/j.finel.2011.12.006.

[10] M. W. Arndt and S. M. Arndt, "with a Temporary-Use Rear Tire and a Run-Flat Rear Tire," *Engineering*, vol. 2006, no. 724, 2006.

[11] L. W. L. Houben, "Run Flat Tires Versus Conventional Tires," vol. 2006, no. September, p. 47, 2006.

[12] W. W. Gardetto, “Advanced high load, quick change run flat system for pneumatic wheeled vehicles,” *SAE Tech. Pap.*, no. 724, 2005, doi: 10.4271/2005-01-0532.

[13] W. Gardetto, D. Gorsich, A. Kurec, J. Mabesa, and D. Murray, “Emissive signature for HMMWV run flat insert modeling and simulation,” *Model. Simul. Mil. Oper. II*, vol. 6564, p. 65640U, 2007, doi: 10.1117/12.718705.

[14] L. Zang, Y. Cai, B. Wang, R. Yin, F. Lin, and P. Hang, “Optimization design of heat dissipation structure of inserts supporting run-flat tire,” *Proc. Inst. Mech. Eng. Part D J. Automob. Eng.*, vol. 233, no. 14, pp. 3746–3757, 2019, doi: 10.1177/0954407019833562.

[15] L. Zang, X. Wang, C. Wu, F. Teng, and S. Yang, “Analysis of Load Characteristic and Contact Patch Characteristic of Support Insert Run-Flat Tire under Zero-Pressure Condition,” *Int. J. Automot. Technol.*, vol. 22, no. 5, pp. 1141–1151, Oct. 2021, doi: 10.1007/s12239-021-0101-8.

[16] Z. Liguo, T. Lv, Y. Li, and X. Wang, “TOPOLOGY OPTIMIZATION OF INSERTS STRUCTURE OF RUN-FLAT TIRE UNDER ZERO-PRESSURE DRIVING CONDITION,” *Int. J. Automot. Technol.*, vol. 24, no. 2, pp. 311–321, 2023, doi: 10.1007/s12239–023–0026–5.

[17] X. Wang, X. Wang, L. Zang, T. Lv, and Y. Li, “Investigation on the characteristics of inserts supporting run- at tire blowout under typical driving conditions considering the camber angle Investigation on the characteristics of inserts supporting run-flat tire blowout under typical driving conditions,” pp. 0–14, 2022.

[18] X. Wang, L. Zang, Z. Wang, F. Lin, and Z. Zhao, “Study on the stability control of vehicle tire blowout based on run-flat tire,” *World Electr. Veh. J.*, vol. 12, no. 3, 2021, doi: 10.3390/wevj12030128.

[19] J. Ejsmont, J. Jackowski, W. Luty, G. Motrycz, P. Stryjek, and B. Ś. Zurek, “Analysis of rolling resistance of tires with run flat insert,” *Key Eng. Mater.*, vol. 597, pp. 165–170,

2014, doi: 10.4028/www.scientific.net/KEM.597.165.

[20] W. V. Mars and A. Fatemi, “A literature survey on fatigue analysis approaches for rubber,” *Int. J. Fatigue*, vol. 24, no. 9, pp. 949–961, 2002, doi: 10.1016/S0142-1123(02)00008-7.

[21] W. V. Mars and A. Fatemi, “Multiaxial fatigue of rubber: Part I: Equivalence criteria and theoretical aspects,” *Fatigue Fract. Eng. Mater. Struct.*, vol. 28, no. 6, pp. 515–522, 2005, doi: 10.1111/j.1460-2695.2005.00891.x.

[22] W. V. Mars, “Multiaxial fatigue of rubber,” p. 517, 2001, [Online]. Available: https://www.proquest.com/docview/304722049

[23] W. V. Mars and A. Fatemi, “Multiaxial fatigue of rubber: Part II: Experimental observations and life predictions,” *Fatigue Fract. Eng. Mater. Struct.*, vol. 28, no. 6, pp. 523–538, 2005, doi: 10.1111/j.1460-2695.2005.00895.x.

[24] K. P. Barbash and W. V. Mars, “Critical Plane Analysis of Rubber Bushing Durability under Road Loads,” *SAE Tech. Pap.*, 2016, doi: 10.4271/2016-01-0393.

[25] W. Nyaaba, E. O. Bolarinwa, and S. Frimpong, “Durability prediction of an ultra-large mining truck tire using an enhanced finite element method,” *Proc. Inst. Mech. Eng. Part D J. Automob. Eng.*, vol. 233, no. 1, pp. 161–169, 2019, doi: 10.1177/0954407018795278.

[26] W. V. Mars, G. Paudel, J. D. Suter, and C. G. Robertson, “Incremental, Critical Plane Analysis of Standing Wave Development, Self-Heating, and Fatigue during Regulatory High-Speed Tire Testing Protocols,” *Tire Sci. Technol.*, vol. 49, no. 3, pp. 172–205, 2021, doi: 10.2346/tire.20.190219.

[27] C. Liang, Z. Gao, S. Hong, G. Wang, B. M. Kwaku Asafo-Duho, and J. Ren, “A Fatigue Evaluation Method for Radial Tire Based on Strain Energy Density Gradient,” *Adv. Mater. Sci. Eng.*, vol. 2021, 2021, doi: 10.1155/2021/8534954.

[28] Endurica LLC, “Endurica CL User documentation.” 2023.

[29] A. G. Thomas, “Rupture of Rubber. V. Cut Growth in Natural Rubber Vulcanizates,” *Rubber Chem. Technol.*, vol. 32, no. 2, pp. 477–489, 1959, doi: 10.5254/1.3542412.

[30] G. J. Lake and P. B. Lindley, “Cut growth and fatigue of rubbers. II. Experiments on a noncrystallizing rubber,” *J. Appl. Polym. Sci.*, vol. 8, no. 2, pp. 707–721, 1964, doi: 10.1002/app.1964.070080212.

[31] G. J. Lake and P. B. Lindley, “The mechanical fatigue limit for rubber,” *J. Appl. Polym. Sci.*, vol. 9, no. 4, pp. 1233–1251, 1965, doi: 10.1002/app.1965.070090405.

[32] W. V Mars and A. Fatemi, “A Phenomenological Model for the Effect of R Ratio on Fatigue of Strain Crystallizing Rubbers,” *Rubber Chem. Technol.*, vol. 76, no. 5, pp. 1241–1258, Nov. 2003, doi: 10.5254/1.3547800.

[33] S. Mahadevan, “Developing a Vehicle Hydroplaning Simulation using Abaqus and CarSim,” 2016.

[34] *STANDARDS MANUAL*. The European Tyre and Rim Technical Organisation. [Online]. Available: http://www.etrto.org

[35] *ENGINEERING DESIGN INFORMATION*. The European Tyre and Rim Technical Organisation. [Online]. Available: http://www.etrto.org

[36] “Hyperelastic Behavior of Rubberlike Materials,” ABAQUS Theory Manual. [Online]. Available: https://docs.software.vt.edu/abaqusv2024/English/?show=SIMACAEMATRefMap/simamat-c-hyperelastic.htm

[37] “Fitting of rubber test data,” ABAQUS Benchmarks Manual. [Online]. Available: https://docs.software.vt.edu/abaqusv2023/English/?show=SIMACAEBMKRefMap/simabmk-c-rubberfit.htm

[38] “Steady-State Transport Analysis.” [Online]. Available: https://docs.software.vt.edu/abaqusv2024/English/?show=SIMACAEANLRefMap/simaanl-c-steadystatetransport.htm

[39] “Steady-state rolling analysis of a tire,” ABAQUS Example Problems. [Online]. Available: https://abaqus-docs.mit.edu/2017/English/SIMACAEEXARefMap/simaexa-c-rollingtire.htm#simaexa-c-rollingtire-t-bibliography-c1

9 Appendix

9.1 MATLAB code for resizing tire

```
clear all;
% Import mesh
    full_text = readlines('175_70_R14.inp');

% Extract nodal data from text
    tempstart = strfind(full_text,"*Node");
    tempend = strfind(full_text,"*Element");
    for n=1:length(tempstart)
        if (tempstart{n}==1)
            start_i=n+1;
        end
        if (tempend{n}==1)
            end_i=n-1;
            break
        end
    end
    nodestext=full_text(start_i:end_i);
    allnodes=[];
    for n=1:length(nodestext)
        allnodes = [allnodes;str2num(nodestext(n))];
    end

% Extract dimension parameters
    origin=[0,0];
    x=allnodes(:,2);y=allnodes(:,3);
    % Compute the size of model
        xmin=min(x);xmax=max(x);
        ymin=min(y);ymax=max(y);
        section_width=abs(ymax-ymin);
        section_height=abs(xmax-xmin);

% Scale and offset
    xscale=6/7;yscale=1.025;xoffset=0.0536;yoffset=0;
    x_updated=(x-xmin)*xscale+xmin+xoffset;
    %[a,b]=(y<=0);
    %y_updated=(y-ymax)*yscale+ymax+yoffset;
    y_updated=y*yscale;
    allnodes_updated=[allnodes(:,1),x_updated,y_updated];

% Write new mesh file
    % Prepare text
        nodestext=[];
        for n=1:length(allnodes_updated);
            nodestext=[nodestext;strjoin(string(allnodes_updated(n,:)),",")];
        end

        filetext=[full_text(1:start_i-1);nodestext;full_text(end_i+1:end)];

    % Write to .inp file
        fid = fopen('temp.inp','w');
        fprintf(fid,'%s\n',filetext{:});
        fclose(fid);
```

9.2 MATLAB code for creating analytical rims with integrated rigid run-flat inserts

```
% Specify width and height of insert
    w=[0.040,0.030];
    h=[0.080:-0.005:0.070];
% Import original rim definition (14 inch)
    rim_text = readlines('RIM_5JX14.inp');
    rim_text(4)="*SURFACE,TYPE=SEGMENTS,NAME=RIM_SURFACE,FILLET RADIUS=0.002";
% Import AXI file to modify
    axi_text = readlines('AXI.inp');

% Extract point where straight line starts from rim definition
tempstart=str2double(strsplit(rim_text(9),','));tempend=str2double(strsplit(rim_text(10),','))
;
    start_cord=tempstart(2:3);
    end_cord=tempend(2:3);

%% Run loop to create insert files
for m=1:length(w)
    wtemp=w(m);
    % Compute the start point of insert
        x_insert_start=interp1([end_cord(2);start_cord(2)],[end_cord(1);start_cord(1)],wtemp);
    for n=1:length(h)
        htemp=h(n);
        % Compute the end point of insert
            x_insert_end=start_cord(1)+htemp;
        % Edit heading of the file
            rim_text(1)=string(['*** 5JX14 RIM WITH
',num2str(2*wtemp*1000),'X',num2str(htemp*1000),' mm INSERT ***']);
        % Start defining insert geometry
            file_text=[];
            temp=string(['LINE,',num2str(x_insert_start),',',num2str(wtemp)]);
            file_text=[file_text;temp];
            temp=string(['LINE,',num2str(x_insert_end),',',num2str(wtemp)]);
            file_text=[file_text;temp];
            temp=string(['LINE,',num2str(x_insert_end),',',num2str(-wtemp)]);
            file_text=[file_text;temp];
            temp=string(['LINE,',num2str(x_insert_start),',',num2str(-wtemp)]);
            file_text=[file_text;temp];
        % Create new folder and write rim+insert input file
            new_rim_text=[rim_text(1:9);file_text;rim_text(11:end)];
            temp_dirname=['INSERT_',num2str(2*wtemp*1000),'X',num2str(htemp*1000)];
            mkdir(temp_dirname);

temp_insertfilename=['RIM_5JX14_INSERT_',num2str(2*wtemp*1000),'X',num2str(htemp*1000),'.inp']
;
            fid = fopen([temp_dirname,'/',temp_insertfilename],'w');
            fprintf(fid,'%s\n',new_rim_text{:});
            fclose(fid);
        % Write AXI file
            axi_text(6)=string(['*Include, Input=',temp_insertfilename]);
            fid = fopen([temp_dirname,'/','AXI.inp'],'w');
            fprintf(fid,'%s\n',axi_text{:});
            fclose(fid);
```